An integrated hydrodynamic model for runoff-generated debris flows with novel formulation of bed erosion and deposition

Xia, Xilin; Jarsve, Kristine Thorkildsen; Dijkstra, Tom; Liang, Qiuhua; Meng, Xingmin; Chen, Guan

DOI:
10.1016/j.enggeo.2023.107310

Document Version
Publisher's PDF, also known as Version of record

Citation for published version (Harvard):
Xia, X, Jarsve, KT, Dijkstra, T, Liang, Q, Meng, X & Chen, G 2023, 'An integrated hydrodynamic model for runoff-generated debris flows with novel formulation of bed erosion and deposition', *Engineering Geology*, vol. 326, 107310. https://doi.org/10.1016/j.enggeo.2023.107310

Engineering Geology 326 (2023) 107310

Contents lists available at ScienceDirect

Engineering Geology

journal homepage: www.elsevier.com/locate/enggeo

An integrated hydrodynamic model for runoff-generated debris flows with novel formulation of bed erosion and deposition

Xilin Xia [a,*], Kristine Thorkildsen Jarsve [b], Tom Dijkstra [b], Qiuhua Liang [b], Xingmin Meng [c], Guan Chen [c]

[a] School of Engineering, University of Birmingham, Birmingham, UK
[b] School of Architecture, Building and Civil Engineering, Loughborough University, Loughborough, UK
[c] School of Earth Sciences, Lanzhou University, Lanzhou, China

ARTICLE INFO

Keywords:
Debris flow
Numerical modelling
erosion and deposition
Depth-averaged model
Godunov-type finite volume method
Stiff source term

ABSTRACT

Debris flow is one of the most common geohazards in mountainous regions, posing significant threats to people, property and infrastructure. Among different types of debris flows, runoff-generated debris flows are attributed to rain storms, which provide abundant runoff that entrain large quantities of bed material, resulting in the formation of a solid-liquid current known as a debris flow. One of the keys to effectively simulating runoff-generated debris flows is modelling the erosion-deposition process. The commonly used approach for formulating erosion and deposition, although constrained by physics, suffers from a singularity in the presence of vanishing velocity, which poses a major challenge for practical applications. It is also argued that the deposition rate cannot be represented by simply reversing the sign of the erosion rate. To address these two issues, we have developed a depth-averaged debris flow model with a novel method of calculating the erosion-deposition rate. We have demonstrated that the singularity is due to the non-linear erosion-deposition term but quickly disappears while the flow converges to the equilibrium that is defined by the classic Takahashi's formula. To resolve the non-linearity and avoid the singularity, an implicit method within a Godunov-type finite volume framework has been proposed. An additional parameter is introduced to differentiate the erosion rate from the deposition rate. The model is validated against several test cases, including a real-world debris flow event. Satisfactory results are obtained, demonstrating the model's simulation capability and potential for wider applications such as risk assessment and impact-based early warning.

1. Introduction

Debris flow is a phenomenon in which poorly sorted sediment, agitated and saturated with water, surges down slopes driven by gravity (Iverson, 1997). It is one of the most common geohazards in mountainous regions. Because of debris flows' long running distances and large velocities, they hold enormous damaging power and pose significant threats to people, property and infrastructure.

There are usually two mechanisms of debris flow initiation. In the first mechanism, debris flows may initiate from shallow landslides, which are triggered by increases in pore water pressure at a slip surface, become flow-like and channelise (Iverson, 1997; Iverson and Denlinger, 2001; Montgomery et al., 2009; Baum et al., 2010; Hungr et al., 2014). In the other mechanism, debris flow initiation is attributed to runoff from low-permeability surfaces during rain storms, which entrain large quantities of loose bed material, forming a debris flow (Cannon et al., 2001; Berti and Simoni, 2005; Larsen et al., 2006; Coe et al., 2008; Gregoretti and Dalla Fontana, 2008). Because of climate change, both rainfall frequency and intensity are expected to increase and thus increasing the frequency of runoff-generated debris flow events (Fuchs et al., 2013; Cui et al., 2021).

Numerical models are essential for managing risk from debris flows. They can be used for risk assessment and impact-based early warning of debris flows by quantifying the run-out distance and velocities. Among all the types of models, depth-averaged models are most common for real-world applications. Because the horizontal dimensions are usually much larger than the vertical dimension, the full 3D governing equations can be integrated along the vertical direction to reduce to 2D equations to significantly reduce computational demand and achieve satisfactory accuracy. In the last few decades, numerous depth-averaged

* Corresponding author.
E-mail address: x.xia.1@bham.ac.uk (X. Xia).

https://doi.org/10.1016/j.enggeo.2023.107310
Received 14 November 2022; Received in revised form 20 September 2023; Accepted 2 October 2023
Available online 5 October 2023

models for debris flows have been developed and applied, (e.g., Iverson and Denlinger (2001); Armanini et al. (2009); van Asch et al. (2014); An et al. (2022); Chen and Zhang (2015); Frank et al. (2015)).

A key challenge in simulating runoff-generated debris flows is formulating and numerically calculating the erosion-deposition process, which is a critical controlling factor for the volume and mobility of debris flow (Dietrich and Krautblatter, 2019; Gregoretti et al., 2019; Zheng et al., 2021). Approaches for modelling erosion-deposition processes can be put into two categories. The first approach is empirical. Takahashi (1978) derived the formula for equilibrium debris flow concentration, i.e., the transport capacity, by balancing gravity and friction forces. An empirical erosion-deposition formula was then proposed based on the difference between the actual concentration and the equilibrium concentration. Egashira et al. (2001) derived their erosion-deposition formula based on the difference between the actual bed slope and the equilibrium bed slope corresponding to the sediment concentration. Armanini et al. (2009) did not explicitly include an erosion-deposition term. Instead, they plugged Takahashi's capacity formula into the transport equation, assuming the concentration is at equilibrium locally. McDougall and Hungr (2005) expressed the erosion-deposition rate in terms of the flow depth, flow velocity, the total eroded/deposited volume, and the flow path length. Frank et al. (2015) defines erosion using a maximum potential erosion depth and a specific erosion rate. Gregoretti et al. (2019) calculated the erosion-deposition rate based on the slope and velocity. The second approach for modelling erosion-deposition processes is process-based. Fraccarollo and Capart (2002) derived an erosion-deposition rate formula based on the jump condition of mass and momentum across the flow-bed boundary. Medina et al. (2008) extended the equation to 2D conditions for real-world debris flow simulations. Iverson and Ouyang (2015) further extended the formula to consider bulk density contract and dilatancy effect at the eroding boundary.

Although the process-based approach provides a strong physical constraint on formulating the erosion-deposition rate, it suffers from a major limitation. Because the velocities appear in the denominator as will later be shown in Eq. (4), the erosion-deposition rate becomes singular in the presence of vanishing velocity, e.g., when the flow starts or stops. This poses a major challenge for implementing this approach in models for practical applications. To address this issue, some models, e.g., Ouyang et al. (2015b); An et al. (2022), have introduced a threshold velocity, below which the erosion/deposition rate becomes zero. In a more sophisticated approach, Pudasaini and Fischer (2020) introduced an additional variable of drifting velocity. By linking the flow velocity to the drifting velocity, which is in turn expressed as shear stresses, the erosion-deposition rate becomes non-singular. Another issue that has not been fully addressed is the contrast between erosion and deposition. Although the deposition process can be modelled by reversing the sign of the erosion rate, which is a common approach (Pudasaini and Fischer, 2020; Iverson and Ouyang, 2015; Ouyang et al., 2015b), some researchers argue that deposition may not necessarily happen when the sign of the erosion rate is reversed. Instead, they argue that an additional condition for deposition is that the flow velocity must be below a certain threshold (Tai and Kuo, 2008). In other words, it is likely that rather than being a gradual process of reversal of erosion, deposition happens more suddenly when the flow velocity has significantly reduced.

To address the challenges mentioned above for practical debris flow simulations, we developed a debris flow model with a novel method of calculating erosion-deposition rate. We first demonstrated the existence of the equilibrium concentration, which is equivalent to Takahashi's sediment transport capacity, even when the process-based approach is adopted. We have then shown that the singularity in the presence of vanishing velocity can be avoided by using an implicit numerical scheme for calculating the source term in a Godunov-type finite volume framework. To consider the difference between erosion and deposition, we have introduced two additional tuning factors. As a result, the model is able to mimic the likely phenomenon in which deposition happens suddenly when flow velocity has significantly reduced. The rest of the paper is organised as follows: section 2 introduces the governing equations; Section 3 presents the new erosion-deposition model; Section 4 presents the details of the new numerical scheme; three test cases including a theoretical case, a laboratory-scale case and a real-world case are presented in section 5; and a conclusion is drawn in section 6.

2. Depth-averaged governing equations for debris flow

The two-dimensional shallow water equations (SWEs) are usually used to model surface water flows such as river flows and flash floods, assuming that the horizontal dimensions are much larger than the vertical dimension. The 2D SWEs can also be applied to simulating runoff-generated debris flows by incorporating erosion-deposition processes and volumetric change of sediment. Following the same approach of Guan et al. (2014), Li and Duffy (2011) and Ouyang et al. (2015b), the governing equations can be written in a matrix form as

$$\frac{\partial \boldsymbol{q}}{\partial t}+\frac{\partial \boldsymbol{f}}{\partial x}+\frac{\partial \boldsymbol{g}}{\partial y}=\boldsymbol{S}_b+\boldsymbol{S}_f+\boldsymbol{S}_e \tag{1}$$

where (x,y) defines two-dimensional Cartesian coordinates (as illustrated in Fig. 1), $\mathbf{q}$ contains the flow variables, $\mathbf{f}$ and $\mathbf{g}$ are the flux terms along x- and y- directions, $\mathbf{S}_b$ are the slope source terms, $\mathbf{S}_f$ is the friction source terms, and $\mathbf{S}_e$ is the source terms related to erosion, deposition and rainfall. They are expressed as

$$\mathbf{q}=\begin{bmatrix} h \\ hu \\ hv \\ hC \\ z \end{bmatrix} \mathbf{f}=\begin{bmatrix} hu \\ hu^2+\frac{1}{2}gh^2 \\ huv \\ huC \\ 0 \end{bmatrix} \mathbf{g}=\begin{bmatrix} hv \\ huv \\ hv^2+\frac{1}{2}gh^2 \\ hvC \\ 0 \end{bmatrix} \tag{2}$$

$$\boldsymbol{S}_b=\begin{bmatrix} 0 \\ -gh\frac{\partial z}{\partial x} \\ -gh\frac{\partial z}{\partial y} \\ 0 \\ 0 \end{bmatrix} \boldsymbol{S}_f=\begin{bmatrix} 0 \\ \frac{\tau_{bx}}{\rho} \\ \frac{\tau_{by}}{\rho} \\ 0 \\ 0 \end{bmatrix} \boldsymbol{S}_e=\begin{bmatrix} E+i \\ -\frac{(\rho_s-\rho_f)gh^2}{2\rho}\frac{\partial C}{\partial x}+\frac{(\rho_0-\rho)uE}{\rho} \\ -\frac{(\rho_s-\rho_f)gh^2}{2\rho}\frac{\partial C}{\partial y}+\frac{(\rho_0-\rho)vE}{\rho} \\ (1-p)E \\ -E \end{bmatrix} \tag{3}$$

in which g is the gravity, h is the flow height, u and v are the x- and y-direction velocities, C is the volumetric concentration of the sediment, z is the bed height, τ_{bx} and τ_{by} are the resistance stresses along x- and y-directions, which are caused by the friction between the flow and the bed, ρ_s is the solid density, ρ_f is the fluid density, ρ is the mixture density,

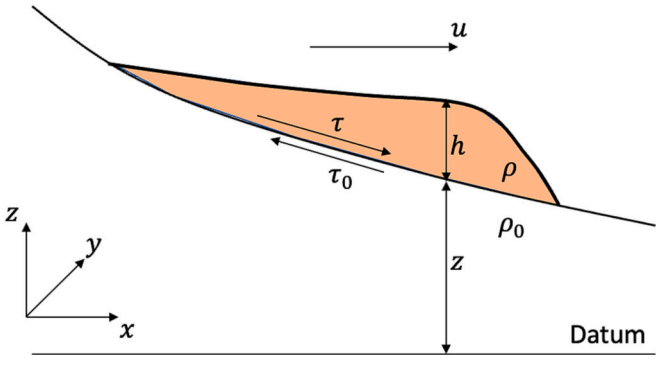

Fig. 1. Definition of key variables for the model.

ρ_0 is the bed material density, p is the bed material porosity, E is the erosion-deposition rate, and i is the excess precipitation rate.

3. Erosion-deposition model

In this section, we will introduce the mathematical formulation of the erosion-deposition terms. We will also discuss the interplay between bed slope, friction and erosion-deposition, which will then lead to the discussion of how the singularity in the presence of vanishing velocities can be avoided.

3.1. Generic formulation of erosion-deposition rate

In this work, the rate for erosion and deposition takes the form of

$$E = \frac{\tau - \tau_0}{\rho_0 \sqrt{u^2 + v^2}} \tag{4}$$

where τ is the friction stress between the flow and the bed, and τ_0 is the threshold stress for the erosion to happen. This formula can be used for both erosion and deposition. If τ is greater than τ_0, $\frac{\partial z}{\partial t} = -E$ becomes negative. This means the bed height decreases therefore the bed material is being eroded. If τ becomes smaller than τ_0, $\frac{\partial z}{\partial t}$ becomes positive. This means the bed height increases therefore the sediment is being deposited.

Firstly proposed by Fraccarollo and Capart (2002), this formulation is derived from the mass and momentum conservation across the boundary between the moving material of debris flow and the static bed material. This formula was then extended by Iverson and Ouyang (2015) to take into account the dilatancy of the bed material. Because this formulation is considered to have more physical basis compared with other formulations, it has been adopted in several debris flow or landslide runout models, e.g., (Ouyang et al., 2015a; Ouyang et al., 2015b; Shen et al., 2019; An et al., 2022; Van Den Bout et al., 2022).

3.2. Singularity in the presence of vanishing velocity and equilibrium state

While this formulation is widely used in debris flow simulations, there is a long-standing issue that is yet to be solved. In Eq. (4), the velocity appears in the denominator. Therefore, the erosion-deposition term is divergent in the presence of vanishing velocity. This can be problematic for numerical simulations as a divergent term causes numerical instability. A pragmatic solution is introducing a threshold velocity. If the velocity is smaller than the threshold velocity then the erosion-deposition term is set as zero, e.g., in Ouyang et al. (2015a); Shen et al. (2020). This is problematic because when the flow is slowing down, the material should deposit and therefore the erosion-deposition term is not zero. In addition, it is difficult to decide the threshold value of the velocity, which may introduce additional uncertainty to the simulations.

With the velocity appearing in the denominator, the erosion-deposition term can be a typical stiff source term that relaxes the flow to the equilibrium state if the frictional stress τ and the threshold stress for erosion τ_0 are carefully chosen. In this work, to take into account both turbulent stresses and frictional stresses, which may be dominant for stony-type debris flows as suggested by (Takahashi et al., 2007), the Manning's formula and the Mohr-Coulomb friction term are combined in τ_{bx} and τ_{by} as

$$\tau_{bx} = \rho g n^2 h^{-1/3} u \sqrt{u^2 + v^2} + (\rho_s - \rho_f) g h C \tan\phi_d \frac{u}{\sqrt{u^2 + v^2}} \tag{5}$$

$$\tau_{by} = \rho g n^2 h^{-1/3} v \sqrt{u^2 + v^2} + (\rho_s - \rho_f) g h C \tan\phi_d \frac{v}{\sqrt{u^2 + v^2}} \tag{6}$$

where n is Manning's coefficient and ϕ_d is the dynamic friction angle to characterise the Mohr-Coulomb friction between the flow and the bed. Combining τ_{bx} and τ_{by}, τ is obtained as

$$\tau = \rho g n^2 h^{-1/3} (u^2 + v^2) + (\rho_s - \rho_f) g h C \tan\phi_d \tag{7}$$

The threshold stress for erosion τ_0 is given as

$$\tau_0 = (\rho_s - \rho_f) g h C \tan\phi_s \tag{8}$$

where ϕ_s is the static friction angle to characterise the Mohr-Coulomb friction of the bed material.

To determine the Mohr-Coulomb friction, we have assumed that the hydrostatic force normal to the bed surface is the same as the debris flow weight along the vertical depth, i.e., gh. This assumption is acceptable if the slope is mild (10–20°), which is true for most debris flow channels, and in those cases the error is small and uncertainties from other sources can be greater. If the slope is steep, the hydrostatic force is different from the weight along the vertical depth (Gregoretti, 2008), therefore the error can be significant. In order to consider the effect of large slopes, the governing equations can be extended following the principles outlined in Xia and Liang (2018a).

We then consider a one-dimensional uniform flow for simplicity and impose the following equilibrium conditions

$$gh \frac{\partial z}{\partial x} = \frac{\tau_{bx}}{\rho} \tag{9}$$

$$\tau_{bx} = \tau_0 \tag{10}$$

which effectively enforces steady flow without erosion or deposition. By substituting Eqs. (5) and (8) into Eqs. (9–10), the corresponding concentration C_∞ can be obtained as

$$C_\infty = \frac{\rho_f \frac{\partial z}{\partial x}}{(\rho_s - \rho_f)(\tan\phi_s - \frac{\partial z}{\partial x})} \tag{11}$$

Indeed this is the transport capacity formula proposed by Takahashi (1978) for debris flow modelling. As shown by our analysis, the governing equations with the deposition-erosion term Eq. (4) recovers the classic Takahashi's formula for debris flow concentration, which is suggested by various experimental studies, e.g., (Lanzoni et al., 2017), to be valid for mature debris flows that usually occur at slopes greater than 15–16°. The values 15–16° are also confirmed by the field work of (Simoni et al., 2020) where 15° is the limit value between the occurrence of deposition and erosion processes.

For the equilibrium state to exist, ϕ_d must be smaller than ϕ_s. During the entrainment process, it is possible that both flow depth and velocity will increase. In this case, the shear stress τ in Eq. (7) will increase. The threshold shear tress τ_0 in Eq. (8) will also increase and can increase more because we have assumed $\phi_d < \phi_s$. Because E is based on $\tau - \tau_0$, E can become 0 and the flow can reach equilibrium. If $\phi_d > \phi_s$, τ will always be greater than τ_0. The equilibrium cannot be reached because E is always positive. $\phi_d < \phi_s$ is however a valid assumption. As is stated in Bagnold (1966) in his experiments, the increase of grain inertia leads to a reduction of dynamic friction coefficient, which is defined as the ratio between normal and shear stresses.

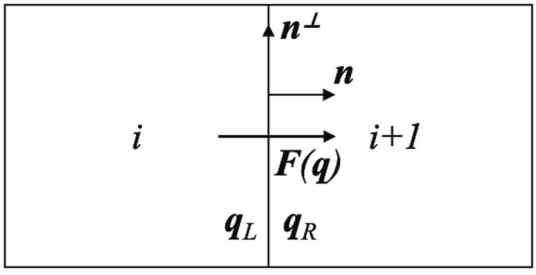

Fig. 2. Definition of local Riemann problem.

The above analysis is based on a relatively simple rheology, but can still be true for more complex rheology such as the viscous rheology. As long as the friction source terms can be divided into two parts, i.e., the velocity-independent Mohr-Coulomb term and velocity-strengthening terms, the equilibrium concentration may still be recovered using the same method of analysis. Exploring the effects of more complex rheology is however out of the scope of the current work.

Although the model converges to Takahashi's formula for debris flow concentration, the model is different from the models that adapt to the transport capacity immediately, e.g., (Armanini et al., 2009), which may fail to provide reliable results at lower sloping angles (Gregoretti et al., 2016). Our model does not enforce the flow to adapt locally to the transport capacity. Instead, it calculates the erosion and deposition rate explicitly based on the difference of basal shear stress and shear strength, therefore can simulate the transient processes of erosion and deposition from the onset of the flow till the convergence to the steady state.

The existence of the well-defined equilibrium state gives a clear physical meaning to the singularity of the erosion-deposition term, which is essentially a stiff relaxation term that forces the flow to converge to the equilibrium state defined by Takahashi's formula. Imagining the flow starting from zero velocity and zero concentration on a slope, as the flow accelerates, the gravity will eventually be balanced by the friction; and as the material is being eroded, the threshold of erosion will also increase as the sediment concentration increases, and eventually balance the friction to result in flow that neither erode or deposit. These processes happen simultaneously and highly non-linearly. The singularity of the erosion-deposition term reflects the fact that the erosion rate is large at the beginning but quickly decreases while the flow converges to the equilibrium. To effectively resolve the non-linearity of the erosion-deposition process, we have proposed a novel implicit numerical method to integrate the erosion-deposition term. We will discuss this in detail in section 4.4.

3.3. Distinction between erosion and deposition

It has been argued that deposition may differ fundamentally from erosion (Issler, 2014). One reason is that the newly deposited material may have distinct mechanical properties such as the internal friction angle. In this work, we take a pragmatic approach to consider the different rates of erosion and deposition. The new erosion-deposition rate is given as

$$E = \begin{cases} \alpha \dfrac{\tau - \tau_0}{\rho_0 \sqrt{u^2 + v^2}} & \text{if} \tau > \tau_0 \\ \beta \dfrac{\tau - \tau_0}{\rho_0 \sqrt{u^2 + v^2}} & \text{if} \tau \le \tau_0 \end{cases} \tag{12}$$

in which α and β are two non-dimensional tuning factors to alter the erosion and deposition rates separately. The introduction of α and β gives a pragmatic yet straightforward way to take into account the difference between the erosion and deposition rates resulting from various factors including the difference in internal friction angles. As we will show later in section 5.2.1, by choosing a small β, our model can also mimic the phenomenon that the deposition only happens when the flow velocity has significantly reduced, as is observed by Tai and Kuo (2008). Although there are no clear physical explanations for the values of α and β yet, our numerical experiments and sensitivity analysis will show how varying α and β will change the debris flow volume and erosion-deposition patterns, therefore informing how the values for these two parameters may be chosen.

4. Numerical scheme

The governing equations are solved using a first-order Godunov-type finite volume method. In this section, we will present the numerical scheme being used to solve the governing equations with a focus on discretising the new erosion-deposition term.

4.1. Finite volume discretisation

The time-marching scheme for the first-order Godunov-type finite volume method is given as

$$\mathbf{q}_i^{n+1} = \mathbf{q}_i^n - \frac{\Delta t}{\Omega_i} \sum_{k=1}^{N} \mathbf{F}_k(\mathbf{q}_i^n) l_k + \Delta t \left(\mathbf{S}_{bi}^n + \mathbf{S}_{fi}^{n+1} + \mathbf{S}_{ei}^{n+1} \right) \tag{13}$$

where the superscript n is the time step, Δt is the time step length, i is the cell index, k is the index of cell edges ($N = 4$ for rectangular grid), l_k is the length of cell edge k, and Ω_i is the cell area, $\mathbf{F}_k(\mathbf{q})$ contains the fluxes normal to the cell edge. Herein, the fluxes $\mathbf{F}(\mathbf{q})$ and slope source term $\mathbf{S}_b$ are calculated explicitly, while the friction term $\mathbf{S}_f$ and the erosion-deposition term $\mathbf{S}_e$ are computed semi-implicitly.

4.2. Discretisation of interfacial fluxes and slope source terms

In this work, the flux terms $\mathbf{F}_k(\mathbf{q}) = \mathscr{F}(\mathbf{q}_L, \mathbf{q}_R)$, in which $\mathbf{q}_L$ and $\mathbf{q}_R$ are the Riemann states, is calculated using an HLLC Riemann solver. Firstly, a local Riemann problem needs to be defined by projecting flow variables onto the local coordinate direction defined at the cell interface:

$$\mathbf{q}_L = \begin{bmatrix} h_L \\ [h\mathbf{v}]_L \cdot \mathbf{n} \\ [h\mathbf{v}]_L \cdot \mathbf{n}^\perp \\ [hC]_L \end{bmatrix} \mathbf{q}_R = \begin{bmatrix} h_R \\ [h\mathbf{v}]_R \cdot \mathbf{n} \\ [h\mathbf{v}]_R \cdot \mathbf{n}^\perp \\ [hC]_R \end{bmatrix} \tag{14}$$

where $[h\mathbf{v}] = ([hu], [hv])$ is the unit-width discharge vector, $\mathbf{n}$ and $\mathbf{n}^\perp$ are the basis vectors (see Fig. 2), with $\mathbf{n}$ being (1,0), (0,1), (−1,0), (0,−1) and $\mathbf{n}^\perp$ being (0, 1), (−1, 0), (0, −1), (0, 1) respectively for the east, north, west and south cell interfaces.

Once the Riemann variables are obtained, the fluxes can be calculated by the HLLC Riemann solver, for which the details can be found in the Appendix and also Toro (2001). The required Riemann states are obtained using the surface reconstruction method (SRM) as proposed by Xia et al. (2017) apart from the additional conservative variable hC. This scheme is chosen because it can robustly capture shock waves and deal with complex real-world topography. SRM firstly reconstructs the water surface elevations at the left and right-hand sides of a given cell interface. Considering two adjacent cells, the cell for updating, i, and its neighbour $i+1$, the reconstructed water surface elevations (denoted by η) are

$$\begin{cases} \eta_L = \eta_i + max[0, min(z_{i+1} - z_i - \delta z, \eta_{i+1} - \eta_i)] \\ \eta_R = \eta_{i+1} + max[0, min(z_i - z_{i+1} + \delta z, \eta_i - \eta_{i+1})] \end{cases} \tag{15}$$

where

$$\delta z = z_{i+1/2+} - z_{i+1/2-} \tag{16}$$

in which $z_{i+1/2-}$ and $z_{i+1/2+}$ are the bed elevations at the left and right-hand sides of the cell interface, which are interpolated from the corresponding cell-centre values using a slope limited method as

$$z_{i+1/2-} = z_i + \mathbf{r}_i \nabla z_i \quad , \quad z_{i+1/2+} = z_{i+1} + \mathbf{r}_{i+1} \nabla z_{i+1} \tag{17}$$

where $\mathbf{r}$ is the vector from the cell centre to the cell edge, and $\nabla \mathbf{z}$ is the slope-limited gradient. In this work, the widely used minmod slope limiter is adopted.

The bed elevations at the left and right-hand sides of the cell interface are then redefined using the reconstructed surface elevation and the corresponding water depth as

$$\begin{cases} z_L = \eta_L - h_i \\ z_R = \eta_R - h_{i+1} \end{cases} \tag{18}$$

which are then used to define a single bed elevation at the cell interface as

$$z_f = max(z_L, z_R) \equiv max(z_i, z_{i+1}) \tag{19}$$

based on which the Riemann states of the flow depth are defined as

$$\begin{cases} h_L = max\left(0, \eta_L - z_f\right) \\ h_R = max\left(0, \eta_R - z_f\right) \end{cases} \tag{20}$$

The Riemann states for hu and hC are the defined as

$$\begin{cases} [hu]_L = h_L u_i, & [hv]_L = h_L v_i, & [hC]_L = h_L C_i \\ [hu]_R = h_R u_{i+1}, & [hv]_R = h_R v_{i+1}, & [hC]_R = h_R C_{i+1} \end{cases} \tag{21}$$

where $u_i = [hu]_i/h_i$ and $C_i = [hC]_i/h_i$ (similarly for u_{i+1}, v_i, v_{i+1} and C_{i+1} are the cell-centred velocities and concentrations.

These Riemann states are then used to calculate the numerical fluxes in Eq. (13) using an HLLC Riemann solver, for which the details are given in the Appendix. The bed slope source terms are then calculated as

$$\mathbf{S}_{bi} = \begin{pmatrix} 0 \\ \dfrac{1}{\Omega_i}\displaystyle\sum_{k=1}^{N} \frac{1}{2} g\left(h_i + h_{L,k}\right)\left(z_i - \overline{z}_{f,k}\right)\mathbf{n}_k l_k \\ 0 \\ 0 \end{pmatrix} \tag{22}$$

where $h_{L,k}$ is the left Riemann state of the flow depth at cell edge 'k', and $\overline{z}_{f,k}$ is defined as

$$\overline{z}_f = z_f - \Delta z \tag{23}$$

$$\begin{cases} \Delta z = max\left(0, z_f - \eta_i\right) & if \quad h_{i+1} < \varepsilon_h \\ \Delta z = max\left(0, min\left(\delta z, z_f - \eta_i\right)\right) & if \quad h_{i+1} >= \varepsilon_h \end{cases} \tag{24}$$

in which $\varepsilon_h = 10^{-10}$ is a small value to define a dry cell. The present flux and slope discretisation schemes automatically preserve still water conditions and ensure non-negative water depth for simulations involving wetting and drying over terrain with complex topography (Xia et al., 2017).

4.3. Discretisation of friction terms

In this work, we take a two-step method to compute the friction terms. In the first stage, Manning's friction term is calculated using the fully-implicit method proposed by Xia and Liang (2018b). This scheme is adopted because it correctly calculates the velocity required for local equilibrium between friction and gravity.

To begin with the calculation, we first update the unit-width discharges with the flux and slope source terms.

$$m_x = q_x^n + \Delta t A_x \tag{25}$$

$$m_y = q_y^n + \Delta t A_y \tag{26}$$

in which $q_x = hu$ and $q_y = hv$ are the $x-$ and $y-$ direction unit-width discharges, and A_x and A_y represent the momentum (second and third) components of $-\frac{1}{\Omega_i}\sum_{k=1}^{N}\mathbf{F}_k(\mathbf{q}^n)l_k + \mathbf{S}_{bi}^n$.

Then the unit-width discharges are further updated as

$$\begin{bmatrix} q_x^{n+1/2} \\ q_y^{n+1/2} \end{bmatrix} = D \begin{bmatrix} m_x \\ m_y \end{bmatrix} \tag{27}$$

where

$$D = \begin{cases} 1 & if \quad M < 10^{-10} \\ \dfrac{1 - \sqrt{1 + 4M}}{-2M} & if \quad M \geq 10^{-10} \end{cases} \tag{28}$$

in which

$$M = \Delta t g n^2 (h^*)^{-4/3} \sqrt{\left(\frac{m_x}{h^*}\right)^2 + \left(\frac{m_y}{h^*}\right)^2} \tag{29}$$

In Eq. (29), h^* is calculated by updating h^n as

$$h^* = h^n + \Delta t A_h \tag{30}$$

with A_h as the mass (first) component of the flux terms $-\frac{1}{\Omega_i}\sum_{k=1}^{N}\mathbf{F}_k(\mathbf{q}^n)l_k$. If h^* is smaller than 10^{-10}, both $q_x^{n+1/2}$ and $q_y^{n+1/2}$ are set as 0 to avoid instability.

In the second stage, the Mohr-Coulomb friction term is calculated using an explicit method. The unit-width discharges are updated as

$$\begin{bmatrix} q_x^* \\ q_y^* \end{bmatrix} = \begin{bmatrix} q_x^{n+1/2} \\ q_y^{n+1/2} \end{bmatrix} - \frac{\Delta t\left(\rho_s - \rho_f\right) g [hC]^*}{\rho\sqrt{\left(u^{n+1/2}\right)^2 + \left(v^{n+1/2}\right)^2}} \begin{bmatrix} u^{n+1/2} \\ v^{n+1/2} \end{bmatrix} \tag{31}$$

in which $u^{n+1/2} = q_x^{n+1/2}/h^*$, $v^{n+1/2} = q_y^{n+1/2}/h^*$, and $[hC]^*$ is calculated by updating h^n as

$$[hC]^* = [hC]^n + \Delta t A_{hC} \tag{32}$$

with A_{hC} as the sediment (fourth) component of the flux terms $-\frac{1}{\Omega_i}\sum_{k=1}^{N}\mathbf{F}_k(\mathbf{q}^n)l_k$. ρ is calculated using the concentration $C^* = [hC]^*/h^*$. In our calculations, the second term in Eq. (31) is capped so that q_x and q_y may reduce to zero but never changes sign as the Mohr-Coulomb friction terms never reverse the flow.

4.4. Discretisation of erosion-deposition terms

In this work, a semi-implicit method is devised to handle vanishing velocities in the erosion-deposition term. The implicit scheme is based on the following time-marching formula for h.

$$h^{n+1} = h^* + k\frac{\tau^* - \tau_0}{\rho_0\sqrt{(u^*)^2 + (v^*)^2}}\frac{1}{1-p} \tag{33}$$

in which in which $u^* = [hu]^*/h^*$ and $v^* = [hv]^*/h^*$, k is chosen as α or β as defined by Eq. (12) depending on whether erosion or deposition is happening.

τ^* is calculated using known variables as

$$\tau^* = \rho g n^2 (h^*)^{-1/3}\left[\left(u^{n+1/2}\right)^2 + \left(v^{n+1/2}\right)^2\right] + \left(\rho_s - \rho_f\right) g [hC]^* tan\phi_d \tag{34}$$

We then define the pseudo fluid depth as

$$h_f^* = h^* - \frac{[hC]^*}{1-p} \tag{35}$$

supposing hC in Eq. (8) can be found from the difference between h_f^* and h^{n+1}, τ_0 is then expressed as

$$\tau_0 = (1-p)\left(\rho_s - \rho_f\right) g\left(h^{n+1} - h_f^*\right) tan\phi_s \tag{36}$$

because h at the next time step is being used, this formula effectively leads to an implicit scheme. The value of k has to be decided before calculating h^{n+1}, which can be done by comparing τ^* against τ_0^* defined as

$$\tau_0^* = \left(\rho_s - \rho_f\right) g [hC]^* tan\phi_s \tag{37}$$

where $\tau^* > \tau_0^*$ leads to $k = \alpha$ whilst $\tau^* \le \tau_0^*$ leads to $k = \beta$.

Substituting Eq. (36) into Eq. (33), the final expression for h^{n+1} can be derived by some algebraic manipulations as

$$h^{n+1} = \frac{\rho_0 h^* k^{-1}\sqrt{(u^*)^2 + (v^*)^2} + \Delta t(\tau^* + \tau_1)}{\rho_0 k^{-1}\sqrt{(u^*)^2 + (v^*)^2} + \Delta t(1-p)(\rho_s - \rho_f) g tan\phi_s} \tag{38}$$

in which

$$\tau_1 = h_f^*(1-p)(\rho_s - \rho_f) g tan\phi_s \tag{39}$$

As long as $\rho_s > \rho_f$, i.e., the debris is heavier than water, the term $\Delta t(1-p)(\rho_s - \rho_f) g tan\phi_s$ is positive, therefore the denominator in Eq. (38) is also positive. As a result, there is no singularity herein.

After obtaining h^{n+1}, $[hC]^{n+1}$ can be obtained as

$$[hC]^{n+1} = [hC]^* + (1-p)\left(h^{n+1} - h^*\right) \tag{40}$$

and the new bed elevation z^{n+1} is calculated as

$$z^{n+1} = z^n - h^{n+1} + h^* \tag{41}$$

The final unit-width discharges can be obtained as

$$\begin{bmatrix} q_x^{n+1} \\ q_y^{n+1} \end{bmatrix} = \begin{bmatrix} q_x^* \\ q_y^* \end{bmatrix} - \Delta t \frac{g\left(h^{n+1}\right)^2(\rho_s - \rho_f)}{2\rho} \begin{bmatrix} \frac{\partial C}{\partial x} \\ \frac{\partial C}{\partial y} \end{bmatrix} - \frac{(\rho_0 - \rho)\left(h^{n+1} - h^*\right)}{\rho} \begin{bmatrix} u^* \\ v^* \end{bmatrix} \tag{42}$$

where $\frac{\partial C}{\partial x}$ and $\frac{\partial C}{\partial y}$ are calculated using central difference method based on $C^{n+1} = [hC]^{n+1}/h^{n+1}$, which is also used for calculating ρ.

4.5. Summary of the solution procedure

At each time step, the procedure of solving the governing equations can be summarised as below:

1. Explicitly evaluate the flux terms and bed slope source terms as described in section 4.2;
2. Integrate the flux terms to get h^*, hC^*, m_x and m_y using Eqs. (30), (32), (25) and (26);
3. Integrate the Manning's friction terms to get $q_x^{n+1/2}$ and $q_y^{n+1/2}$ using Eq. (27);
4. Integrate the Mohr-Coulomb friction terms to get q_x^* and q_y^* using Eq. (31);
5. Evaluate the value of k using Eqs. (34) and (37);
6. Integrate the erosion-deposition terms to get h^{n+1} using Eq. (38);
7. Integrate the erosion-deposition terms to get $[hC]^{n+1}$ using Eq. (40);
8. Integrate the erosion-deposition terms to get z^{n+1}, q_x^{n+1} and q_y^{n+1} using Eqs. (41–42);
9. Update the flow variables and go to the next time step.

4.6. Stability criterion

For solving the depth-averaged equations using an explicit finite volume method, the time step size Δt must be constrained by the Courant-Friedrich-Levy (CFL) condition which is given as

$$\Delta t = CFL \min_i \left(\frac{\Delta x}{\sqrt{u_i^2 + v_i^2} + \sqrt{g h_i}} \right) \tag{43}$$

where Δx is the cell size, and CFL is the Courant number ranging from 0 to 1. As the numerical treatment of the erosion-deposition terms addresses the stiffness and avoided any singularity, they do not impose any further constraint on the time step size.

5. Test cases

In this section, a few test cases are simulated to validate the new debris flow model.

5.1. 1-D uniform flow on slopes

We first consider a case of 1-D uniform flow on slopes. This is to test the model's capability to converge the flow to the correct equilibrium state even starting from zero velocity. For this test case, the initial conditions are $h = 1.0$ m, $C = 0$ and $u = 0$ m/s. We set the parameters as Manning's $n = 0.035$ sm$^{-1/3}$, static friction coefficient $tan\phi_s = 0.6$, dynamic friction coefficient $tan\phi_b = 0.5$, density of the solids $\rho_s = 2600$ kg/m^3, density of the water $\rho_f = 1000$ kg/m^3, porosity $p = 0.4$, and the tuning factors $\alpha = 1.0$ and $\beta = 1.0$. Four different slope ratios, i.e., 0.05, 0.1, 0.15 and 0.2, are chosen for this test case. Because the flow is uniform, all the terms including partial derivatives with respect to x are set as 0. A constant time step of 0.1 s is used. The results are presented in Fig. 3. For all four different slope ratios, the simulated concentration converges to the equilibrium concentration, which is calculated using Eq. (11). Simulations with larger slopes reach the equilibrium state more slowly, which may be explained by the larger equilibrium concentrations. The results confirm the model's capability to not only handle vanishing velocities, but also recover the correct equilibrium state. This is important for practical applications because it is usually the equilibrium concentration, or in other words, the transport capacity, that controls the total volume of sediment, and consequently the deposition area.

5.2. Takahashi's flume experiment

To further test the numerical model we used the flume experiment by Takahashi et al. (1992). This experiment consists of a long, narrow flume (10 cm) with an inclination of 18° (Fig. 4). A 2 m wide flood board with an inclination of 5° is connected to the flume. A 10 cm deep and 3 m long erodible bed layer is positioned 5.5 m upstream of the flume's outlet. The erodible material has a mean particle size (d_{50}) of 3.08 mm and a density of 2650 kg/m^3. A constant water flow with a discharge of 600 cm^3 s^{-1} was supplied for 20 s to generate the debris flow (Takahashi et al., 1992).

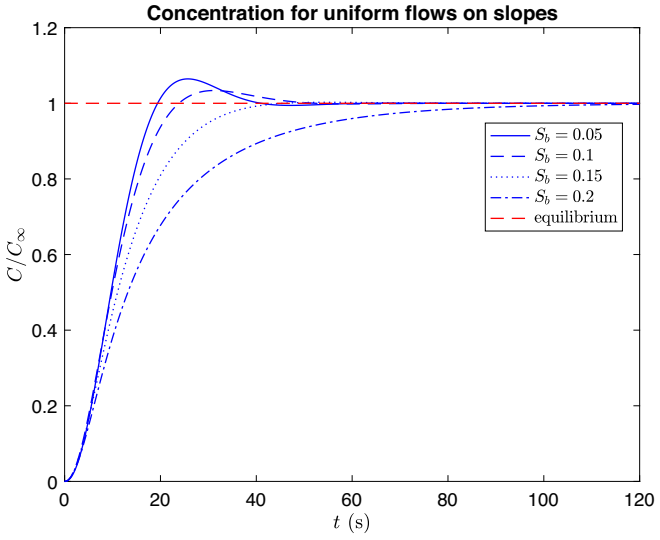

Fig. 3. Changes of concentration against time for flow on slopes with different inclinations.

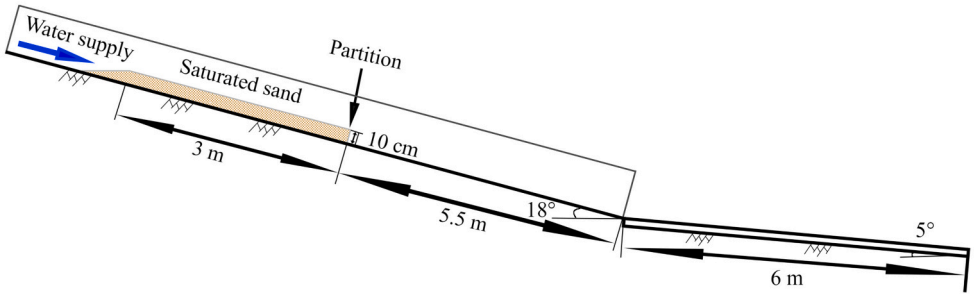

(a) The flume experiment by Takahashi et al. (1992) seen from the side.

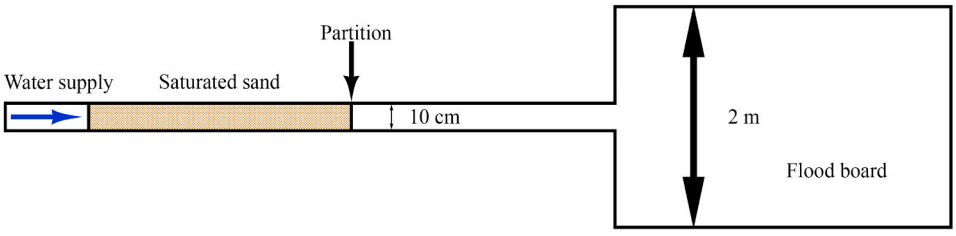

(b) The flume experiment by Takahashi et al. (1992) seen from above.

Fig. 4. Set-up of Takahashi et al. (1992) flume experiment. Figure is redrawn from Chen and Zhang (2015).

The parameters used in this simulation were $\rho_f = 1000$ kg/m^3, $\rho_s = 2650$ kg/m^3, $p = 0.4$, and $n = 0.018$ sm$^{-1/3}$. The particle size was set to 3.08 mm – the mean particle size used in the physical experiment by Takahashi et al. (1992). The best values for static and dynamic coefficients, i.e., $tan\phi_s$ and $tan\phi_d$, and α and β were found by trial and error. To do so, two sets of simulations were carried out: 1) The friction parameters, $tan\phi_s$ and $tan\phi_d$, were varied while α and β were kept constant at $\alpha = 1$ and $\beta = 0.01$. The values for static friction were set to $tan\phi_s = [0.58, 0.6, 0.62, 0.64, 0.66, 0.68, 0.7]$ and the values for dynamic friction were $tan\phi_s = [0.38, 0.4, 0.42, 0.44, 0.46, 0.48, 0.5]$. 2) The tuning factors α and β were varied while the friction parameters were kept constant at $tan\phi_s = 0.62$ and $tan\phi_d = 0.44$. The values for α were set to $[0.01, 0.05, 0.1, 0.5, 1.0, 1.5, 2.0]$ and the values for β were set to $[0.01, 0.05, 0.1, 0.5, 1.0, 1.5, 2.0]$. For each simulation set 49 simulations with different combinations of the parameters were run. Each simulation was run for 60 s.

Comparing the discharge and deposition area from the model with the results from Takahashi et al. (1992), we found that the simulation where $\alpha = 1$, $\beta = 0.01$, $tan\phi_s = 0.62$ and $tan\phi_d = 0.44$ (Fig. 5) gave the results closest to the experimental data. In Fig. 5a the deposition area from the simulation has been plotted. After filtering out deposition material with a height < 5 mm we see that there is a good fit between the modelled deposition (solid surface plot) and the deposition from the physical experiment (contour lines). The modelled deposition area has a slightly rounder, more symmetric shape than the physical experiment by Takahashi et al. (1992) but this is expected because the setup of the experiment could not be perfectly symmetric. The height of the deposition area from the model is also similar to the physical experiment, although a slight difference is found at the flume exit where the modelled deposition shows a height up to 6 cm while the contours from Takahashi et al. (1992) shows a height of 5 cm. Fig. 5b shows the discharges measured at the entrance (blue graph) and exit (orange graph) of the flume compared to the discharges from Takahashi's experiment (symbols). We see that the modelled discharge corresponds well with the discharges from Takahashi et al. (1992).

Satisfactory results for both the modelled deposition area and discharge confirm that the new model is able to capture the essential characteristics of runoff-generated debris flows. The results also confirm the importance of differentiating the erosion and deposition rates. The parameters of $\alpha = 1.0$ and $\beta = 0.01$ indicate that deposition happens at a

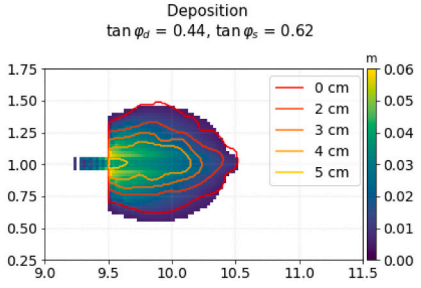

(a) The comparison of the modelled deposition area and the experimental deposition area (contours) from Takahashi et al. (1992)'s flume experiment.

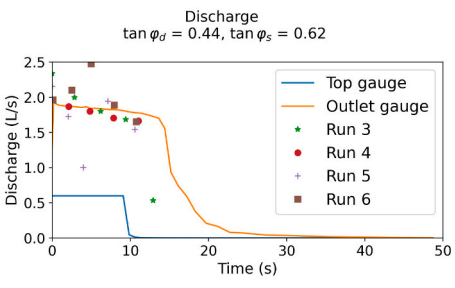

(b) Discharges measured at the entrance (blue) and exit (orange) of the flume compared to the experimental results by Takahashi et al. (1992) (symbols, run 3–6).

Fig. 5. Simulated deposition and discharge compared to the results from Takahashi et al. (1992)'s flume experiment.

much slower rate than erosion.

5.2.1. Sensitivity analysis

We have also conducted a sensitivity analysis to investigate the role of different parameters and inform the choice of parameter values. For the sensitivity analysis, the five parameters α, β, $tan\phi_s$, $tan\phi_d$, and Manning's n were tested using the set-up of Takahashi et al. (1992)'s flume experiment. Following the framework developed by Hussin et al. (2012), each parameter was varied in increments of 10% while the other parameters were kept constant. The base value (100%) for each of the parameters has been listed in Table 1. The changes in peak discharge can be seen in Fig. 6a. We immediately see that the static friction, $tan\phi_s$, is the most sensitive parameter where a decrease of 30% results in an increase in peak discharge of more than 60%. Increasing $tan\phi_s$ also leads to large reductions in discharge. The trends of α, $tan\phi_d$, and Manning's n are very similar and we see that the peak discharge increases when the parameter values are increased. However, α and $tan\phi_d$ appears to be less sensitive than Manning's n. No obvious variations in the results from β can be seen in this plot. The high sensitivity of $tan\phi_s$ is anticipated because it governs the threshold for material erosion. While increasing both $tan\phi_d$ and Manning's n can raise the friction force, this force at the equilibrium state is primarily determined by the slope. As a result, the maximum discharge exhibits less sensitivity to changes in $tan\phi_d$ and Manning's n.

Fig. 6b shows how deposition area changes when the parameters are varied. Once again we see that it is the static friction, $tan\phi_s$, that is the most sensitive. The area changes about 10% for every 10% increase or decrease of the parameter. The area is also highly sensitive to the dynamic friction, $tan\phi_d$, though this sensitivity is lower than for the static friction. The deposition area is also sensitive to α, most likely because this alters how much sediment is entrained, which will affect the volume of deposition. Again, no variations in the result can be seen for β.

The model's sensitivity to β could not be seen in Fig. 6 as the changes were too small, and thus appears as a straight horizontal line when the values were changed in increments of 10%. We therefore tested β separately on the *log* scale. Fig. 7a shows how the peak discharge changes with varying β. While the change in peak discharge is quite small, we see that the discharge increases with decreasing β and that the discharge is converging when β becomes small. This is to be expected as higher values of β will cause more material to be deposited sooner, i.e. in the flume, before reaching the flume outlet. The deposition area (Fig. 7b) increases rapidly for decreasing β-values before decreasing and then slowly increasing again as β decreases. The general trend of increase in deposition area with decreasing β is expected as a lower β allows the material to flow further before depositing. The most interesting observation is that the deposition area appears to converge while β is small. This can be explained by the fact that the velocity is in the denominator of the deposition rate term; as β becomes small, the deposition rate is only significant enough when the velocity is small. In other words, deposition only happens when the flow is close to full stoppage if β is small enough. By choosing a small β, the flow effectively becomes static as a block rather than gradually losing its mass along the path.

In summary, the sensitivity analysis reveals that the model is most sensitive to the static friction coefficient, $tan\phi_s$, in terms of both peak discharge and deposition area. The dynamic friction, $tan\phi_d$, also significantly impacts the deposition area, but its influence on peak discharge is less pronounced. Sensitivity to changes in α and Manning's n is relatively lower, with α showing the least sensitivity among the two. The model's sensitivity to the parameter β is minimal when β is varied linearly. When β varies on a logarithmic scale, its effect on discharge remains low, but its impact on the deposition area is considerable.

Table 1
Base values (100%) used in the sensitivity analysis of the model.

Parameter	α	β	$tan\phi_s$	$tan\phi_d$	Manning's n
Base value	1	0.01	0.7	0.4	0.02 $sm^{-1/3}$

5.2.2. Discussions on values of α and β

Takahashi's experiment exemplifies typical debris flow gullies, which are characterized by steeper channels merging into flatter deposition basins. Consequently, insights from this experiment can guide parameter selection for real-world case studies. The sensitivity analysis reveals that debris flow volume and deposition area change by a similar percentage as α varies, suggesting that adjusting α around 1 can help fine-tune these aspects. In contrast, β significantly influences deposition patterns, with smaller values (0.001–0.1) leading to deposition mostly in flatter areas, as commonly observed in real-world scenarios. Therefore, it is recommended to choose a β value within the range of 0.001 to 0.1.

5.3. Zhouqu debris flow

To further test the model for real-world cases we simulated the Zhouqu debris flow event in 2010. Zhouqu (Fig. 9) is the county capital in the southern part of Gansu Province, China, located along the Bailong River at the southeastern edge of the Tibetan Plateau and the Longmen and Qinling mountain ranges (Tang et al., 2011). The Indosinian, Yanshan, and Himalayan orogenic periods have significantly affected the region and there are several active faults trending NWW-SSE and NEE-SWW, defining a complex tectonic system (Zhang et al., 2018). The area is characterized by rugged mountains and deeply incised valleys and has a high topographic (relative) relief with elevations ranging from 1200 to over 4000 m. On August 7–8, 2010, a cloudburst precipitation event with an intensity of at least 77 mm/h (Fig. 8) occurred in a set of catchments north of Zhouqu (an intensity of 77.3 mm/h was measured at the nearby Dongshan weather station). This event generated two debris flows that hit the town and resulted in over 1750 fatalities (Dijkstra et al., 2012; Tang et al., 2011; Cui et al., 2013; Yu et al., 2015; Zhang et al., 2018).

The debris flows originated from two different catchments: Sanyanyu and Luojiayu (Fig. 9b, yellow and green polygons respectively in Fig. 9c) which both have outlets in Zhouqu. Old rockfall and landslide deposits that partially or completely blocked the channels at higher elevations in both catchments contributed significant material to the debris flows (Cui et al., 2013; Dijkstra et al., 2012; Tang et al., 2011; Ren et al., 2013). A total of 9 check dams were placed in the Sanyanyu prior to the 2010 event (Fig. 9c) with heights ranging from 6 to 11 m (Xiong et al., 2016).

5.3.1. Model set up

The parameters used in the set-up of the simulation of the 2010 Zhouqu debris flows can be seen in Table 2. The density of the solids was reported to be 2000 kg/m^3 (Hu et al., 2012) and the mean particle size was found to be 10 mm (Xiong et al., 2016). The porosity was kept at 0.4 while Manning's n was set to 0.035 $sm^{-1/3}$. Through calibration, the best static and dynamic friction angles were found to be $tan\phi_s = 0.71$ and $tan\phi_d = 0.45$ while the best α and β values were found to be $\alpha = 1.0$ and $\beta = 0.06$. Because the whole catchment is included in the simulation domain, the simulation is entirely rainfall driven, without an inflow hydrograph as a boundary condition. The rainfall time series recorded at the Dongshan weather station (Fig. 8) was converted to rain intensity and input to the model uniformly across the whole domain. Because there was abundant rainfall for a few days before the debris flow event and the soil moisture was likely to be high, we assumed that the infiltration loss was small. Thus the rain record is taken as the excess rainfall without infiltration. More accurate calculation of runoff can be made by coupling the hydrodynamic model with hydrological models.

The base DEM was updated with the dimensions of the mapped landslide deposits and check dams to accurately replicate the gullies in the model. The erosion raster (Fig. 10), which defines the locations where erosion may occur, was generated based on the eroded areas observed on the KOMPSAT-2 image taken shortly after the event

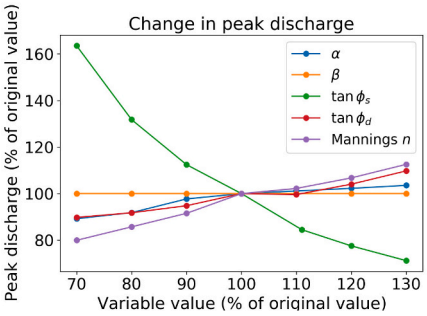

(a) Change in peak discharge with different values of the input parameters α, β, $\tan\phi_s$, $\tan\phi_d$, and Manning's n.

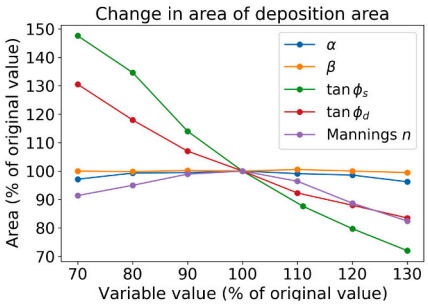

(b) Change in deposition area with different values of the input parameters α, β, $\tan\phi_s$, $\tan\phi_d$, and Manning's n.

Fig. 6. Model sensitivity to changes in the input parameters α, β, $tan\phi_s$, $tan\phi_d$, and Manning's n and their effect on (a) discharge and (b) extent of deposition area.

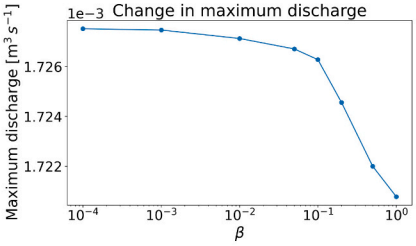

(a) Sensitivity of β in regards to peak discharge plotted on a log-scale.

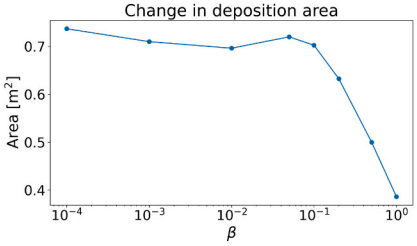

(b) Sensitivity of β in regards to are of the deposition area on a log-scale.

Fig. 7. The sensitivity of the input parameter β and its effect on **a)** peak discharge and **b)** deposition area.

Table 2
Input parameters used in the simulation of the 2010 Zhouqu Debris Flows.

Parameter	ρ_f	ρ_s	Particle diametre	p	Manning's n
Value	1000 kg/m^3	2000 kg/m^3	10 mm	0.4	0.035 sm$^{-1/3}$

(Fig. 13c). Mapped landslide and rockfall deposits (Fig. 9c) were added as additional erodible material. The erosion depths were estimated based on observations from Dijkstra et al. (2012) and Cui et al. (2013), who visited the area shortly after the event.

In the upper catchment, away from the main channels, a maximum erosion depth of 0.5 m was permitted. The upper main channels allowed for erosion depths up to 1 m, while the middle catchment's main channel permitted up to 5 m of material to be eroded. In the lower sections of the catchments, the main channels in the Sanyanyu and Luojiayu allowed

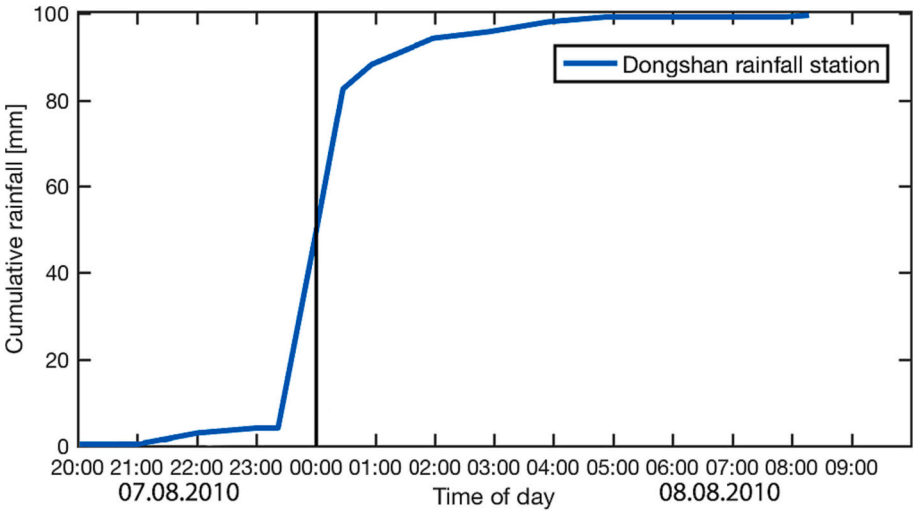

Fig. 8. Cumulative rainfall recorded at the Dongshan rainfall station near Zhouqu in the late evening/early morning of August 7–82,010 (Dijkstra et al., 2012). The vertical black line is used to visually separate the dates 07.08 and 08.08.2010.

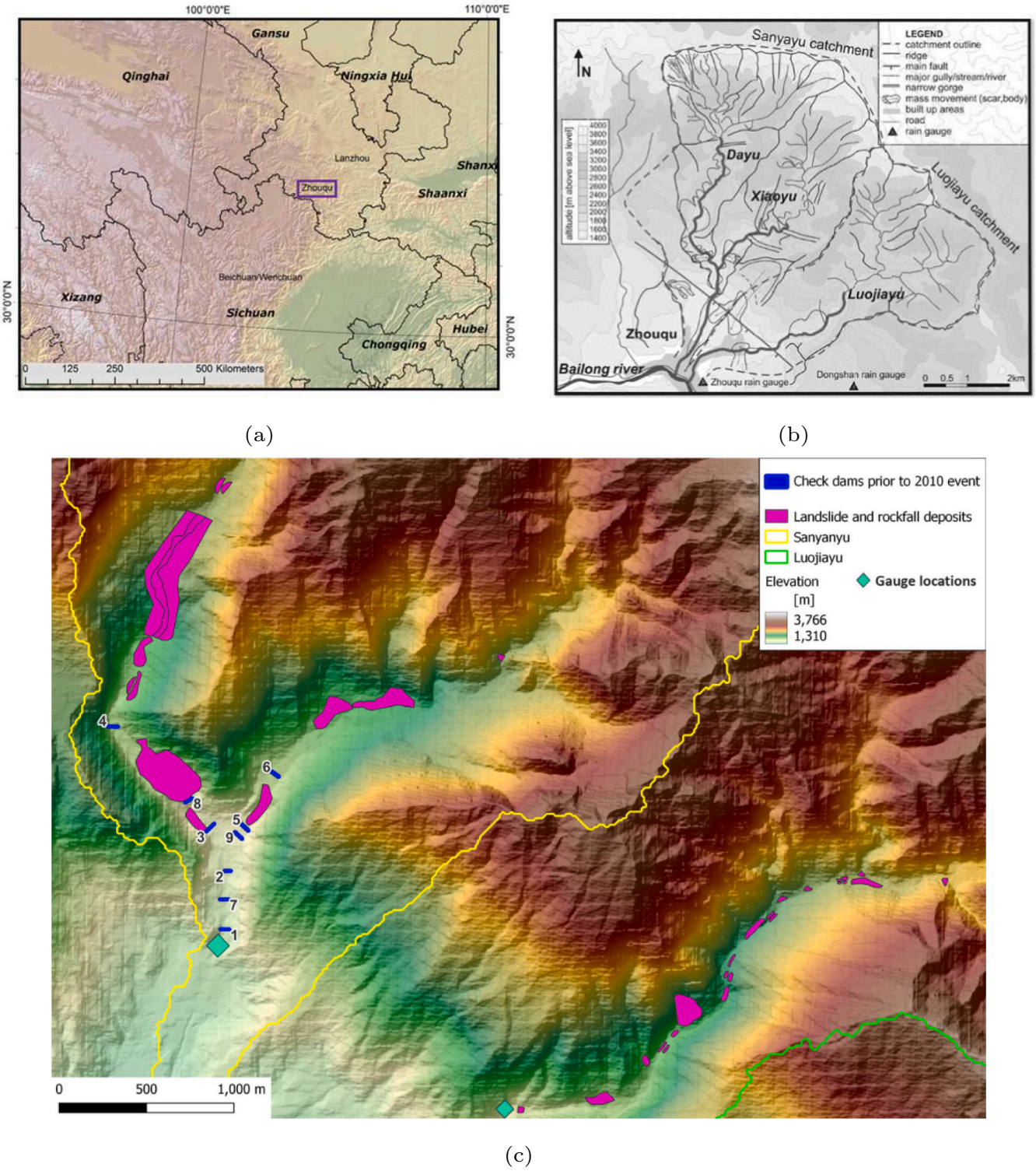

Fig. 9. Location diagrams for the research catchment northeast of Zhouqu. (a) Location of the county town of Zhouqu in southern Gansu (modified after Dijkstra et al. (2014)); (b) the Zhouqu area showing the locations of the Sanyanyu and Luojiayu catchments and the two rain gauges of Zhouqu and Dongshan (after Dijkstra et al., 2012); (c) a detailed view of the lower portions of the Sanyanyu and Luojiayu catchments (outlined in yellow and green, respectively) showing the locations of check dams and valley based landslide and rockfall deposits. (For interpretation of the references to colour in this figure legend, the reader is referred to the web version of this article.)

for erosion of 30 m and 20 m of material, respectively. Lastly, in the deposition areas, up to 5 m of material could be eroded.

The simulations were run using 1) a DEM with a 6 m resolution generated by combining a re-sampled 12.5 m ALOS-PALSAR (Rosenqvist et al., 2007) image with a 6 m resolution DEM generated from contour lines provided by *Gansu Administration of Surveying, Mapping and Geo-information* and 2) the SRTM30 (Farr and Kobrick, 2000) DEM with a resolution of 30 m.

The purpose of running simulations with two distinct DEMs is to examine the impact of using different DEMs from different sources with

varying grid sizes on the model's performance. This comparison is valuable for understanding how the model performs when using both high-resolution, locally sourced DEMs and globally available free DEMs. By doing so, we can better understand the model's broader applicability and potential limitations in different scenarios.

5.3.2. Results

In this section, we present and compare the measured discharges, extent, and flow heights from the simulations using the 6 m and 30 m resolutions DEMs.

Discharge. Fig. 11 presents the simulated solid-liquid mixture discharges from the simulation with a 6 m resolution DEM. The discharges were measured from the simulations on gauges distributed every 6 m (grid size) across the debris channels, close to the exits of the Sanyanyu (Fig. 11a) and the Luojiayu (Fig. 11b) gullies, for which the locations can be seen in Fig. 9. The measured discharges from each gauge were summed to obtain the total discharge for each gully. A sharp rise of discharge can be found at about $t = 10000$ s (167 min) indicating the rapid increase in rainfall intensity (Fig. 8). However, small surges can also be observed at later time steps. The simulated discharge for Luojiayu (Fig. 11b) appears to have many surges. These surges are likely to be caused by rapid entrainment and deposition due to fast flow on steep slopes in areas surrounding the gauges.

In contrast, the 30 m resolution simulation (Fig. 12) shows smoother hydrographs with more prominent peaks, indicating less intense local entrainment and deposition in areas where discharges are gauged. This is not surprising because a larger grid size can result in wider channels and consequently smaller flow velocities. The main flow, which arrives at approximately 12000 s (200 min), comes as two large surges with discharges of approximately 400 $m^{3/s}$. As the flow diminishes after the rainfall has stopped, several smaller surges can be seen before the flow stops completely. The discharge from the Luojiayu (Fig. 12b) has one main surge shortly after 10000 s (167 min) with a peak discharge of about 300 $m^{3/s}$. The discharges for the 30 m simulation are generally smaller than what we observed for the 6 m simulation. This phenomenon could be again attributed to the fact that a larger grid size results in wider channels, particularly upstream, which in turn leads to reduced velocities. Consequently, the overall amount of eroded material is decreased.

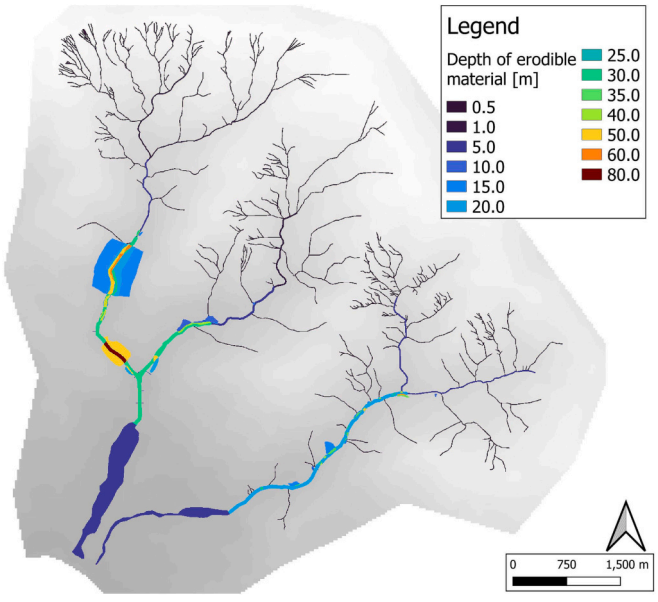

Fig. 10. Spatial distribution of the erosional depths used in the simulations of the 2010 Zhouqu debris flows. The erodible material in the channels has been combined with the erodible landslide and rockfall deposits, and check dams mapped in Fig. 9. This leads to the erosional depths ranging from 0.5 m in the upper bifurcations to 80 m in a section of the channel filled by a massive rockfall deposit. The grey area, which outlines the catchment, had a maximum erodible depth of 0.8m.

Extent. Fig. 13a compares the the deposition (white – red) and erosion (white – blue) from the 6 m simulation and the area of real deposition (yellow outlines). To make the areas clearer, a threshold of ±5cm was used, smaller than which the deposition and erosion area were made transparent. The model result is a close match to the observed deposition, especially for the Sanyanyu (on the left). However, there are a few hollow areas that show neither erosion nor deposition inside the yellow polygon and when the model result is compared to the KOMPSAT-2-image (Dijkstra et al. (2012)) taken shortly after the event (Fig. 13c). This could be due to several factors, such as e.g., the threshold used to display the data or anomalies of the DEM. In the simulation result, erosion can also be found within the yellow polygon, which can be attributed to the fluctuations of heights within the DEM, in which higher areas are more likely to be eroded. Along the inner curve of the Luojiayu (to the right), there are some areas with deposited material separated from the main stream. The thickness of this material is most likely close to 5 cm. It is also possible that this material originates from the hillslopes to the south of the channel. To the south of the yellow polygons, towards the edge of the DEM, substantial deposition has occurred in the model. This area lies in the river channel of the Bailong River which was dammed by the debris flows in 2010. According to Yu et al. (2010); Tang et al. (2011), the height of the sediments damming the river was 10 m. This has been reproduced by our model, where up to 10 m of sediments have been deposited in the Bailong River (Fig. 13a).

The deposition from the 30 m resolution simulation is displayed in Fig. 13b. Again, a threshold of ±5 cm was used to display the area clearer. The extent of modelled deposition and erosion from the 30 m simulation is close to the observed deposition area from the event. While we see the deposition has spread more than the result from the 6 m simulation (Fig. 13a), few hollow areas can be seen within the outlines of the observed deposition area, which could again be caused by fluctuations of DEM heights. At the exit of the Sanyanyu (top of the left deposition area in Fig. 13b) a substantial amount of deposits have accumulated (up to 25 m). This was neither observed in reality nor in the 6 m simulations and is thus likely caused by inaccuracies in the 30 m DEM.

In addition to the visual comparison of the deposition area, we have also calculated the probability of detection (POD) and false alarm ratio (FAR) as described by Ming et al. (2020). The POD, also called hit rate, is given by

$$POD = \frac{\text{hits}}{\text{hits} + \text{misses}} \tag{44}$$

and ranges from 0 to 1, where $POD = 1$ is a perfect result. FAR is given by

$$FAR = \frac{\text{false alarms}}{\text{hits} + \text{false alarms}} \tag{45}$$

and its values also range between 0 and 1, with 0 being the optimal value.

For the 6 m simulation, $POD = 0.85$ and $FAR = 0.27$ which are close to their optimal values of 1 and 0 respectively. The 30 m simulation resulted in a POD of 0.92 and FAR of 0.33, indicating better performance in detecting affected areas, but also higher overestimation. Despite this, both resolutions produced satisfactory results, as verified by visual comparison with the observed extent of the 2010 debris flow event. Ultimately, we conclude that simulations with both DEMs are capable of realistically reproducing the event, with the higher resolution simulation offering slightly better detection while sacrificing some precision in mapping the extent of the affected areas.

Flow heights. The flow heights observed at different time intervals during the 6 m and 30 m resolution simulations are presented in Fig. 14.

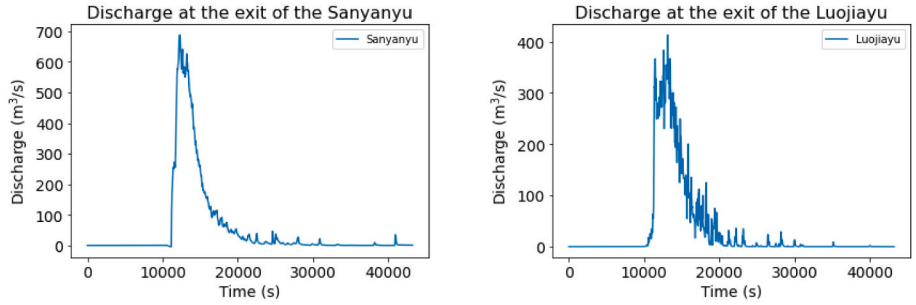

(a) The solid-liquid discharge measured at the exit of the Sanyanyu gully.

(b) The solid-liquid discharge measured close to the exit of the Luojiayu gully.

Fig. 11. Time series of the simulated solid-liquid discharges measured from the 6 m DEM simulation at the a) exit of the Sanyanyu and b) close to the exit of the Luojiayu.

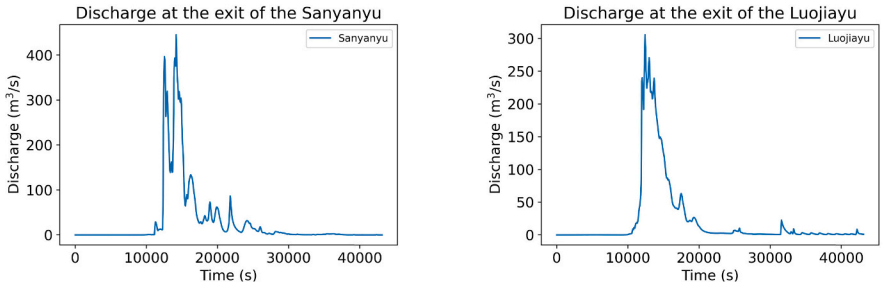

(a) The solid-liquid discharge measured at the exit of the Sanyanyu gully.

(b) The solid-liquid discharge measured close to the exit of the Luojiayu gully.

Fig. 12. Time series of the simulated solid-liquid discharges measured from the 30 m DEM simulation at the a) exit of the Sanyanyu and b) close to the exit of the Luojiayu.

At the initial time of 150 min (panels A), which corresponds to 23:30 (Fig. 8), only a small amount of precipitation has fallen in the catchments, making it challenging to observe the flow, especially in the simulation with 6 m resolution (Fig. 14a). However, due to the coarse grid in the 30 m resolution simulation, the flow is slightly more visible. At the end of the cloudburst event, 210 min later (panels B), i.e., at 00:30 (Fig. 8), we can clearly observe the flow in both catchments. Even after 510 min, at 05:30 (panels C), when precipitation has stopped, the material can still be seen flowing out of the catchments. The flow height remained primarily in the range of 2–6 m, but locally, it could reach up to 15 m due to the check dams or small errors in the DEM. These observations are consistent with gully observations and sediment markings on the buildings in the deposition area (Cui et al., 2013; Tang et al., 2011).

Comparing the flow heights between the 6 m and 30 m resolution simulations, we observe that both simulations follow a similar pattern. However, the debris flow in the 30 m simulation appears to be more visible and less confined in channels, especially upstream. This effect is likely due to the larger grid size and consequent topographic smoothing (Gregoretti et al., 2016, 2019).

Discussions. In summary, both the simulations using a 30 m DEM and 6 m DEM yield realistic results, although variations can be found. In general, for the coarser 30 m simulations, the erosion-deposition patterns and the flow hydrographs are smoother, and less material has been eroded. The difference may be mainly attributed to the difference in grid sizes as coarser DEM smooths out topographic details, making the flow less volatile. It is, however, important to note that the two DEMs are generically different and thus variations in the results may also be attributed to the sampling techniques and survey quality, as well as the grid resolution (Boreggio et al., 2018, 2022). As noted by Stolz and Huggel (2008), the quality and resolution of the DEM need to be carefully selected based on the modelling application. The simulations using both a coarse and high-resolution DEM demonstrate that our model is suitable for both fast and computational inexpensive overviews as well as for more detailed modelling to address specific questions (such as the impact of check dams in a gully).

6. Conclusion

This paper presents in detail an integrated hydrodynamic model for runoff-generated debris flows. The model incorporates erosion-deposition processes and volumetric change of sediment into the 2D SWEs. A novel formulation of bed erosion and deposition is proposed to remove the singularity due to vanishing velocity. By carefully choosing the formulae for the frictional stress and the threshold stress for erosion, the classic Takahashi's formula for debris flow concentration can be recovered from the governing equations when the flow is at an equilibrium state. As a result, the difficulty of removing the singularity of the erosion-deposition term is equivalent to numerically integrating stiff source terms, for which well-established methods exist. Within a first-order Godunov-type finite volume framework, the erosion-deposition source term is calculated implicitly and therefore the correct equilibrium state can be recovered by the model in a numerically stable manner. To account for the difference between the erosion and deposition rates reported in the literature, a tuning factor is multiplied with the erosion and deposition term. The factor takes different values when the flow is in an erosion or deposition regime.

The model is validated by three case studies, including a theoretical test case, a laboratory-scale test case and a real-world debris flow event. It is able to converge to the correct steady flow solution on a 1-D slope

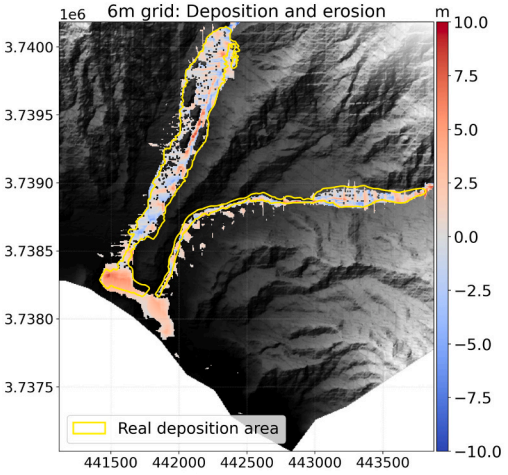

(a) Deposition and erosion from the **6 m** simulation compared to deposition areas (yellow outlines) from the 2010 debris flows in Zhouqu.

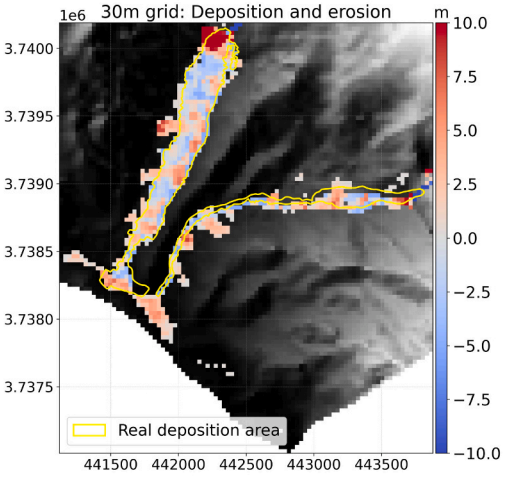

(b) Deposition and erosion from the **30 m** simulation compared to deposition areas (red outlines) from the 2010 debris flows in Zhouqu.

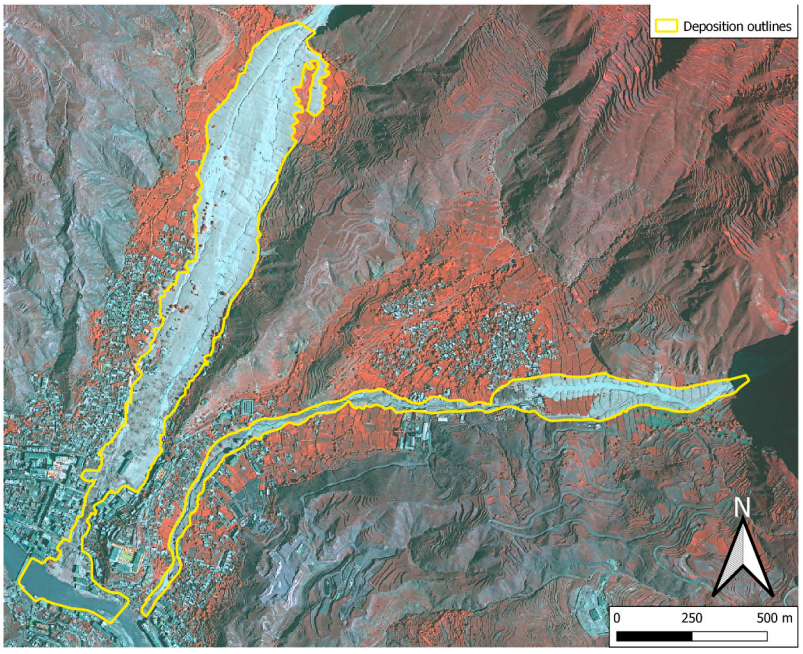

(c) Actual deposition (yellow outlines) from the 2010 debris flows in Zhouqu as seen from a KOMPSAT-2 (Dijkstra et al. (2012)) image taken shortly after the event.

Fig. 13. Modelled erosion and deposition from the simulations using a) a 6 m DEM and b) a 30 m DEM. Figure c) shows the deposition in Zhouqu shortly after the debris flows occurred on 08.08.2010. The deposition area of the *Sanyanyu* can be seen to the left while the deposition area to the right is from the Luojiayu.

even starting at zero velocity, and reproduce both the hydrograph and deposition morphology of Takahashi's debris flow experiment. The parameter sensitivity analysis shows that the model is most sensitive to the static friction coefficient for both peak discharge and the deposition area. And the deposition area seems to converge while the tuning factor for erosion/deposition is small, suggesting that the model can reproduce the deposition mechanism that deposition only happens when the flow is near stoppage. Finally, the model is applied to simulate the 2010 Zhouqu debris flow event in China, using both a locally sourced 6 m DEM and the free SRTM 30 m DEM. For both simulations, the simulated deposition area and the deposition height within the Bailong River agree well with the post-event survey.

In summary, this work has solved a long-standing issue for simulating the erosion/deposition process and developed a model that is able to capture the key aspects of the dynamics of runoff-generated debris flows. The model has the potential to be applied for risk assessment and impact-based early warning of runoff-generated debris flows.

List of symbols

$\mathbf{q}$	Flow variables in the depth-averaged equations
$\mathbf{F}$	Flux through cell interface
$\mathbf{f}$	x-direction flux
$\mathbf{S}_b$	Slope source terms

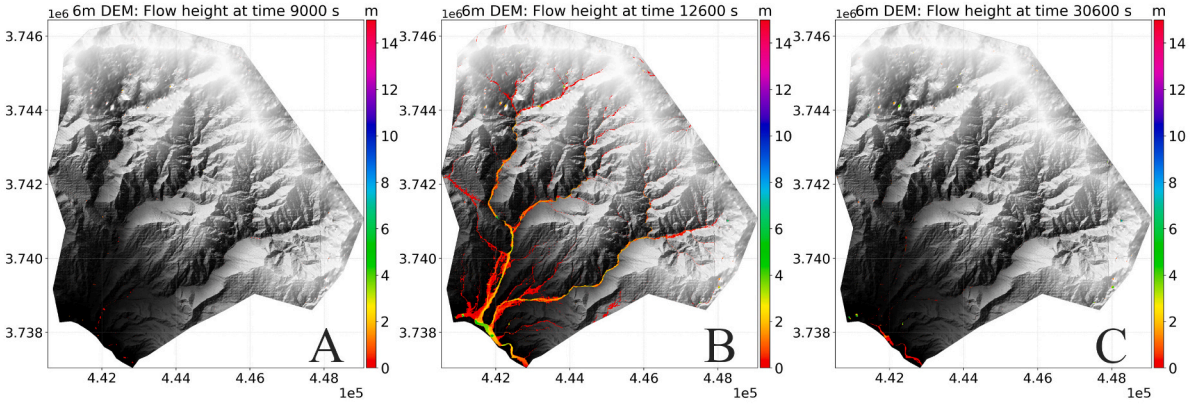

(a) Flow heights captured from the 6 m resolution simulation at **A)** 9000 s (150 minutes), **B)** 12600 s (210 minutes), and **C)** 30600 s (510 minutes) into the simulation. The panels correspond to the rainfall at hours 23:30, 00:30, and 05:30 in the rainfall time series (Figure 8) respectively.

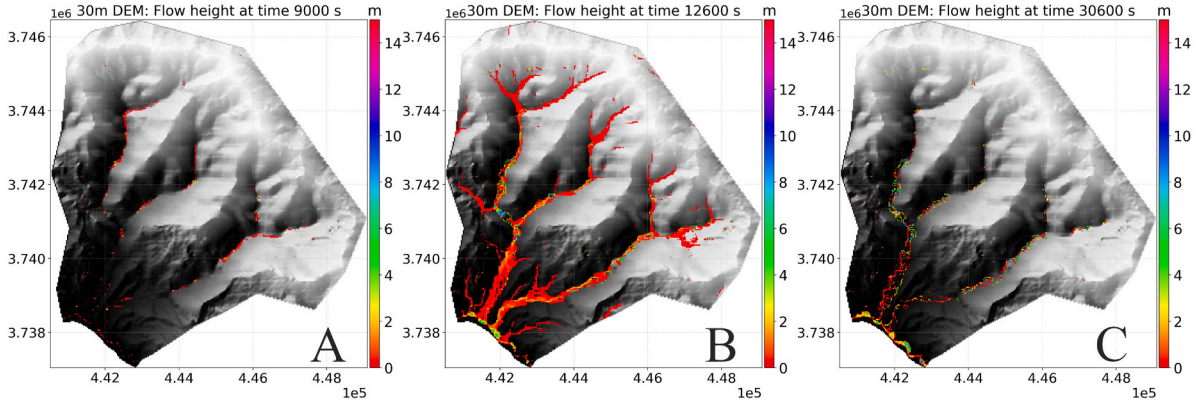

(b) Flow heights captured from the 30 m resolution simulation at **A)** 9000 s (150 minutes), **B)** 12600 s (210 minutes), and **C)** 30600 s (510 minutes) into the simulation. The panels correspond to the rainfall at hours 23:30, 00:30, and 05:30 in the rainfall time series (Figure 8) respectively.

Fig. 14. The simulated flow heights from the 6 m DEM simulation (a) and the 30 m DEM simulation (b).

$\mathbf{S}_f$	Friction source terms
$\mathbf{S}_e$	Source terms of erosion, deposition and rainfall
t	time
x	x-direction
y	y-direction
g	gravity
h	flow height
η	flow surface elevation
u	x-direction velocity
v	y-direction velocity
C	Concentration of sediment
E	Rate of erosion and deposition
τ	Total bed resistance stress
τ_{bx}	Bed resistance stress along x-direction
τ_{by}	Bed resistance stress along y-direction
ρ_s	Solid density
ρ_f	Fluid density
ρ	Mixture density
ρ_0	Bed material density
n	Manning's coefficient
ϕ_d	Dynamic friction angle
ϕ_s	Static friction angle
τ_0	Threshold stress for erosion
C_∞	Equilibrium sediment concentration
α	Tuning factor for erosion
β	Tuning factor for deposition
Ω	cell area
l	cell edge length
$\mathbf{r}$	vector from the cell centre to the cell edge
m_x, m_y	updated unit-width discharges
A_x, A_y	momentum (second and third) components of the flux plus slope source terms
A_h	mass (first) component of the flux terms
A_{hC}	sediment (fourth) component of the flux terms
D, M	intermediate variables for integrating friction terms
$h^*, q_x^*, q_y^*, [hC]^*$	intermediate variables for updating h, q_x, q_y and hC
h_f^*	intermediate fluid depth for integrating erosion/deposition terms
τ^*, τ_1	intermediate variables for integrating erosion/deposition terms
k	factor representing either α or β
Δt	time step size

CFL	Courant number
POD	probability of detection
FAR	False alarm ratio

CRediT authorship contribution statement

Xilin Xia: Writing – review & editing, Writing – original draft, Visualization, Validation, Supervision, Software, Resources, Methodology, Funding acquisition, Conceptualization. **Kristine Thorkildsen Jarsve:** Writing – review & editing, Writing – original draft, Visualization, Validation, Methodology. **Tom Dijkstra:** Writing – review & editing, Supervision, Resources. **Qiuhua Liang:** Writing – review & editing, Supervision, Resources. **Xingmin Meng:** Supervision. **Guan Chen:** Data curation.

Declaration of Competing Interest

The authors declare that they have no known competing financial interests or personal relationships that could have appeared to influence the work reported in this paper.

Data availability

The dataset for Takahashi's flume experiment was obtained by digitising the figures from Takahashi et al. (1992). The 6 m DEM of Zhouqu and the debris flow deposition area were provided by Lanzhou University and may be requested from the authors. The 30 m SRTM DEM for Zhouqu is free and can be downloaded from the USGS website (https://earthexplorer.usgs.gov). The rainfall input for the Zhouqu case study was obtained from (Dijkstra et al., 2012). The debris flow model is implemented as part of the open-source code SynxFlow, which can be downloaded from Github (https://github.com/SynxFlow/SynxFlow).

Acknowledgement

The simulations were supported by the Baskerville Tier-2 HPC, which is funded by the EPSRC and UKRI through the World Class Labs scheme (EP/T022221/1) and the Digital Research Infrastructure programme (EP/W032244/1). Kristine Thorkildsen Jarsve is supported by a scholarship from Loughborough University. We also thank the two anonymous reviewers for their constructive feedback, which has helped to improve this paper.

Appendix A. The HLLC Riemann solver

Taking the x-direction flux $\mathbf{f}$ as an example and considering the first three components in the vector first, the HLLC Riemann solver gives

$$\mathbf{f}_{1,2,3} = \begin{cases} \mathbf{f}_L & 0 \le S_L \\ \mathbf{f}_{*L} & S_L \le 0 \le S_M \\ \mathbf{f}_{*R} & S_M \le 0 \le S_R \\ \mathbf{f}_R & S_R \le 0 \end{cases} \tag{46}$$

in which $\mathbf{f}_L = \mathbf{f}(\mathbf{q}_L)$ and $\mathbf{f}_R = \mathbf{f}(\mathbf{q}_R)$ are calculated from the left and right Riemann states, S_L, S_R and S_M the are characteristic wave speeds. $\mathbf{f}_{*L}$ and $\mathbf{f}_{*R}$ are the fluxes in the left and right middle regions of the HLLC solution structure, calculated as

$$\mathbf{f}_{*L} = \begin{bmatrix} f_{*1} \\ f_{*2} \\ v_L f_{*1} \end{bmatrix} \quad \mathbf{f}_{*R} = \begin{bmatrix} f_{*1} \\ f_{*2} \\ v_R f_{*1} \end{bmatrix} \tag{47}$$

where $v_L = [hv]_L/h_L$ and $c_L = [hC]_L/h_L$ (similarly for v_R and C_R), f_{*1} is the first component of $\mathbf{f}_*$, f_{*2} is the second component of $\mathbf{f}_*$. The HLL fluxes $\mathbf{f}_*$ are provided by the following formula

$$\mathbf{f}_* = \frac{S_R\mathbf{f}_L - S_L\mathbf{f}_R + S_L S_R(\mathbf{q}_R - \mathbf{q}_L)}{S_R - S_L} \tag{48}$$

The formulae for the left and right characteristic wave speeds S_L and S_R are

$$S_L = \begin{cases} u_R - 2\sqrt{gh_R} & h_L = 0 \\ min\left(u_L - \sqrt{gh_L}, u_* - \sqrt{gh_*}\right) & h_L > 0 \end{cases} \tag{49}$$

$$S_R = \begin{cases} u_L + 2\sqrt{gh_L} & h_R = 0 \\ max\left(u_R + \sqrt{gh_R}, u_* + \sqrt{gh_*}\right) & h_R > 0 \end{cases} \tag{50}$$

in which

$$u_* = \frac{1}{2}(u_L + u_R) + \sqrt{gh_L} - \sqrt{gh_R} \tag{51}$$

$$h_* = \frac{1}{g}\left[\frac{1}{2}\left(\sqrt{gh_L} + \sqrt{gh_R}\right) + \frac{1}{4}(u_L - u_R)\right]^2 \tag{52}$$

The middle characteristic wave speed S_M is calculated as

$$S_M = \frac{S_L h_R(u_R - S_R) - S_R h_L(u_L - S_L)}{h_R(u_R - S_R) - h_L(u_L - S_L)} \tag{53}$$

Finally, the fourth component of $\mathbf{f}$, i.e., the sediment flux is given as

$$f_4 = \begin{cases} f_1 C_L & if \ f_1 \geq 0 \\ f_1 C_R & if \ f_1 < 0 \end{cases} \tag{54}$$

where C_L is defined as $[hC]_L/h_L$ (similarly for C_R), and f_1 is the first component of **f**, i.e., the mass flux.

Finally, the flux $\mathbf{F}_k$ on a cell face 'k' can be obtained by projecting **f** back to the global coordinates, it is given as

$$\mathbf{F}_k = \begin{bmatrix} f_1 \\ f_2^* \mathbf{n}_k + f_3^* \mathbf{n}_k^{\perp} \\ f_4 \end{bmatrix} \tag{55}$$

where f_1, f_2, f_3 and f_4 are the three components of **f**.

References

An, H., Ouyang, C., Wang, F., Xu, Q., Wang, D., Yang, W., Fan, T., 2022. Comprehensive analysis and numerical simulation of a large debris flow in the Meilong catchment, China. Eng. Geol. 298 (January), 106546. https://doi.org/10.1016/j.enggeo.2022.106546.

Armanini, A., Fraccarollo, L., Rosatti, G., 2009. Two-dimensional simulation of debris flows in erodible channels. Comput. Geosci. 35 (5), 993–1006. https://doi.org/10.1016/j.cageo.2007.11.008.

Bagnold, R.A., 1966. An Approach to the Sediment Transport Problem from General Physics. USGS Professional Paper, p. 42.

Baum, R.L., Godt, J.W., Savage, W.Z., 2010. Estimating the timing and location of shallow rainfall-induced landslides using a model for transient, unsaturated infiltration. J. Geophys. Res. Earth 115, F03013.

Berti, M., Simoni, A., 2005. Experimental evidences and numerical modeling of debris flow initiated by channel runoff. Landslides 2 (3), 171–182.

Boreggio, M., Bernard, M., Gregoretti, C., 2018. Evaluating the differences of gridding techniques for digital elevation models generation and their influence on the modeling of stony debris flows routing: a case study from rovina di cancia basin (North-eastern Italian alps). Front. Earth Sci. 6, 89.

Boreggio, M., Bernard, M., Gregoretti, C., 2022. Does the topographic data source truly influence the routing modelling of debris flows in a torrent catchment? Earth Surf. Process. Landf. 47 (8), 2107–2129.

Cannon, S.H., Kirkham, R.M., Parise, M., 2001. Wildfire-related debris-flow initiation processes, storm King Mountain, Colorado. Geomorphology 39 (3–4), 171–188.

Chen, H.X., Zhang, L.M., 2015. EDDA 1.0: Integrated simulation of debris flow erosion, deposition and property changes. Geosci. Model Dev. 8 (3), 829–844.

Coe, J.A., Kinner, D.A., Godt, J.W., 2008. Initiation conditions for debris flows generated by runoff at Chalk Cliffs, Central Colorado. Geomorphology 96 (3–4), 270–297.

Cui, P., Zhou, G.G., Zhu, X.H., Zhang, J.Q., 2013. Scale amplification of natural debris flows caused by cascading landslide dam failures. Geomorphology 182, 173–189.

Cui, P., Peng, J., Shi, P., Tang, H., Ouyang, C., Zou, Q., Liu, L., Li, C., Lei, Y., 2021. Scientific challenges of research on natural hazards and disaster risk. Geogr. Sustain. 2 (3), 216–223. https://doi.org/10.1016/j.geosus.2021.09.001.

Dietrich, A., Krautblatter, M., 2019. Deciphering controls for debris-flow erosion derived from a lidar-recorded extreme event and a calibrated numerical model (roßbichelbach, Germany). Earth Surf. Process. Landf. 44 (6), 1346–1361.

Dijkstra, T., Chandler, J., Wackrow, R., Meng, X., Ma, D., Gibson, A., Whitworth, M., Foster, C., Lee, K., Hobbs, P.R.N., Wasowski, J., 2012. Geomorphic controls and debris flows-the 2010 zhouqu disaster, China. In: 11th International Symposium on Landslides and 2nd North American Symposium on Landslides. CRC Press Inc.

Dijkstra, T., Wasowski, J., Winter, M., Meng, X., 2014. Introduction to Geohazards of Central China. Q. J. Eng. Geol. Hydrogeol. 47, 195–199.

Egashira, S., Honda, N., Itoh, T., 2001. Experimental study on the entrainment of bed material into debris flow. Phys. Chem. Earth Part C Solar Terrestr. Planet. Sci. 26 (9), 645–650.

Farr, T.G., Kobrick, M., 2000. Shuttle radar topography mission produces a wealth of data. EOS Trans. Am. Geophys. Union 81 (48), 583–585.

Fraccarollo, L., Capart, H., 2002. Riemann wave description of erosional dam-break flows. J. Fluid Mech. 461, 183–228.

Frank, F., McArdell, B.W., Huggel, C., Vieli, A., 2015. The importance of entrainment and bulking on debris flow runout modeling: examples from the swiss alps. Nat. Hazards Earth Syst. Sci. 15 (11), 2569–2583.

Fuchs, S., Keiler, M., Sokratov, S., Shnyparkov, A., 2013. Spatiotemporal dynamics: the need for an innovative approach in mountain hazard risk management. Nat. Hazards 68 (3), 1217–1241.

Gregoretti, C., 2008. Inception Sediment Transport Relationships at High Slopes. J. Hydraul. Eng. 134 (11), 1620–1629.

Gregoretti, C., Dalla Fontana, G., 2008. The triggering of debris flow due to channel-bed failure in some alpine headwater basins of the Dolomites: analyses of critical runoff. Hydrol. Process. 22, 2248–2263.

Gregoretti, C., Degetto, M., Boreggio, M., 2016. GIS-based cell model for simulating debris flow runout on a fan. J. Hydrol. 534, 326–340. https://doi.org/10.1016/j.jhydrol.2015.12.054.

Gregoretti, C., Stancanelli, L.M., Bernard, M., Boreggio, M., Degetto, M., Lanzoni, S., 2019. Relevance of erosion processes when modelling inchannel gravel debris flows for efficient hazard assessment. J. Hydrol. 568, 575–591.

Guan, M., Wright, N.G., Asce, F., Sleigh, P.A., 2014. 2D Process-based Morphodynamic Model for Flooding by Noncohesive Dyke Breach. J. Hydraul. Eng. 140 (7), 1–12.

Hu, K.H., Cui, P., Zhang, J.Q., 2012. Characteristics of damage to buildings by debris flows on 7 August 2010 in Zhouqu, Western China. Nat. Hazards Earth Syst. Sci. 12 (7), 2209–2217. URL. https://nhess.copernicus.org/articles/12/2209/2012/.

Hungr, O., Leroueil, S., Picarelli, L., 2014. The Varnes classification of landslide types, an update. Landslides 11 (2), 167–194.

Hussin, H.Y., Quan Luna, B., Van Westen, C.J., Christen, M., Malet, J.P., van Asch, T.W. J., 2012. Parameterization of a numerical 2-D debris flow model with entrainment: a case study of the Faucon catchment, Southern French Alps. Nat. Hazards Earth Syst. Sci. 12 (10), 3075–3090.

Issler, D., 2014. Dynamically consistent entrainment laws for depth-averaged avalanche models. J. Fluid Mech. 759, 701–738.

Iverson, R.M., 1997. The physics of debris flows. Rev. Geophys. 35 (3), 245–296.

Iverson, R.M., Denlinger, R.P., 2001. Flow of variably fluidized granular masses across three-dimensional terrain: 1. Columb mixture theory. J. Geophys. Res. 106 (B1), 537–552.

Iverson, R.M., Ouyang, C., 2015. Entrainment of bed material by Earthsurface mass flows: Review and reformulation of depth-integrated theory. Rev. Geophys. 53, 27–58.

Lanzoni, S., Gregoretti, C., Stancanelli, L.M., 2017. Coarse-grained debris flow dynamics on erodible beds. J. Geophys. Res. Earth 122 (3), 592–614.

Larsen, I.J., Pederson, J.L., Schmidt, J.C., 2006. Geologic versus wildfire controls on hillslope processes and debris flow initiation in the Green River canyons of Dinosaur National Monument. Geomorphology 81 (1–2), 114–127.

Li, S., Duffy, C.J., 2011. Fully coupled approach to modeling shallow water flow, sediment transport, and bed evolution in rivers. Water Resour. Res. 47 (3), 1–20.

McDougall, S., Hungr, O., 2005. Dynamic modelling of entrainment in rapid landslides. Can. Geotech. J. 42 (5), 1437–1448.

Medina, V., Bateman, A., Hürlimann, M., 2008. A 2D finite volume model for bebris flow and its application to events occurred in the Eastern Pyrenees. Int. J. Sediment Res. 23 (4), 348–360. https://doi.org/10.1016/S1001-6279(09)60006-8.

Ming, X., Liang, Q., Xia, X., Li, D., Fowler, H.J., 2020. Real-time flood forecasting based on a high-performance 2-D hydrodynamic model and numerical weather predictions. Water Resour. Res. 56, e2019WR02558.

Montgomery, D.R., Schmidt, K.M., Dietrich, W.E., McKean, J., 2009. Instrumental record of debris flow initiation during natural rainfall: Implications for modeling slope stability. J. Geophys. Res. Earth 114 (1), 1–16.

Ouyang, C., He, S., Tang, C., 2015a. Numerical analysis of dynamics of debris flow over erodible beds in Wenchuan earthquake-induced area. Eng. Geol. 194, 62–72. https://doi.org/10.1016/j.enggeo.2014.07.012.

Ouyang, C., He, S., Xu, Q., 2015b. MacCormack-TVD finite difference solution for dam break hydraulics over erodible sediment beds. J. Hydraul. Eng. 141, 1–9.

Pudasaini, S.P., Fischer, J.T., 2020. A mechanical erosion model for two-phase mass flows. Int. J. Multiphase Flow 132, 103416. https://doi.org/10.1016/j.ijmultiphaseflow.2020.103416.

Ren, D., Leslie, L., Lynch, M., Duan, Q., Dai, Y., Shangguan, W., 2013. Why was the August 2010 Zhouqu landslide so powerful? Geogr. Environ. Sustain. 6 (1), 67–79.

Rosenqvist, A., Shimada, M., Ito, N., Watanabe, M., 2007. Alos palsar: a pathfinder mission for global-scale monitoring of the environment. IEEE Trans. Geosci. Remote Sens. 45 (11), 3307–3316.

Shen, W., Li, T., Li, P., Shen, Y., Lei, Y., Guo, J., 2019. The influence of the bed entrainment-induced rheology and topography changes on the propagation of flow-like landslides: a numerical investigation. Bull. Eng. Geol. Environ. 78 (7), 4771–4785.

Shen, P., Zhang, L., Wong, H.F., Peng, D., Zhou, S., Zhang, S., Chen, C., 2020. Debris flow enlargement from entrainment: a case study for comparison of three entrainment models. Eng. Geol. 270 (March), 105581. https://doi.org/10.1016/j.enggeo.2020.105581.

Simoni, A., Bernard, M., Berti, M., Boreggio, M., Lanzoni, S., Stancanelli, L.M., Gregoretti, C., 2020. Runoff-generated debris flows: Observation of initiation conditions and erosion–deposition dynamics along the channel at Cancia (eastern Italian Alps). Earth Surf. Process. Landf. 45 (14), 3556–3571.

Stolz, A., Huggel, C., 2008. Debris flows in the swiss national park: the influence of different flow models and varying dem grid size on modeling results. Landslides 5, 311–319.

Tai, Y.C., Kuo, C.Y., 2008. A new model of granular flows over general topography with erosion and deposition. Acta Mech. 199 (1–4), 71–96.

Takahashi, T., 1978. Mechanical characteristics of debris flow. J. Hydraul. Div. 104 (8), 1153–1169. URL. https://ascelibrary.org/doi/abs/10.1061/JYCEAJ.0005046.
Takahashi, T., Nakagawa, H., Harada, T., Yamashiki, Y., 1992. Routing Debris Flows with Particle Segregation. J. Hydraul. Eng. 118 (11), 1490–1507.
Takahashi, T., Nakagawa, H., Harada, T., Yamashiki, Y., 2007. Routing Debris Flows with Particle Segregation. J. Hydraul. Eng. 118 (11), 1490–1507.
Tang, C., Rengers, N., van Asch, T.W.J., Yang, Y.H., Wang, G.F., 2011. Triggering conditions and depositional characteristics of a disastrous debris flow event in Zhouqu city, Gansu Province, northwestern China. Nat. Hazards Earth Syst. Sci. 11 (11), 2903–2912.
Toro, E.F., 2001. Shock-Capturing Methods for Free-Surface Shallow Flow. John Wiley & Sons, Ltd.
van Asch, T., Tang, C., Alkema, D., Zhu, J., Zhou, W., 2014. An integrated model to assess critical rainfall thresholds for run-out distances of debris flows. Nat. Hazards 70, 299–311. URL. http://link.springer.com/article/10.1007/s11069-013-0810-z.
Van Den Bout, B., Tang, C., Van Westen, C., Jetten, V., 2022. Physically based modeling of co-seismic landslide, debris flow, and flood cascade. Nat. Hazards Earth Syst. Sci. 22 (10), 3183–3209.
Xia, X., Liang, Q., 2018a. A new depth-averaged model for flow-like landslides over complex terrains with curvatures and steep slopes. Eng. Geol. 234 (January), 174–191. https://doi.org/10.1016/j.enggeo.2018.01.011. http://linkinghub.elsevier.com/retrieve/pii/S0013795217306324.
Xia, X., Liang, Q., 2018b. A new efficient implicit scheme for discretising the stiff friction terms in the shallow water equations. Adv. Water Resour. 117 (May), 87–97. https://doi.org/10.1016/j.advwatres.2018.05.004.
Xia, X., Liang, Q., Ming, X., Hou, J., 2017. An efficient and stable hydrodynamic model with novel source term discretization schemes for overland flow and flood simulations. Water Resour. Res. 53, 3730–3759. URL. http://doi.wiley.com/10.1002/2016WR020055.
Xiong, M., Meng, X., Wang, S., Guo, P., Li, Y., Chen, G., Qing, F., Cui, Z., Zhao, Y., 2016. Effectiveness of debris flow mitigation strategies in mountainous regions. Prog. Phys. Geogr. 40 (6), 768–793.
Yu, B., Yang, Y., Su, Y., Huang, W., Wang, G., 2010. Research on the giant debris flow hazards in Zhouqu County, Gansu Province on August 7, 2010. J. Eng. Geol. 437–444.
Yu, G., Zhang, M., Cong, K., Pei, L., 2015. Critical rainfall thresholds for debris flows in Sanyanyu, Zhouqu County, Gansu Province, China. Q. J. Eng. Geol. Hydrogeol. 48 (3–4), 224–233.
Zhang, Y., Meng, X., Jordan, C., Novellino, A., Dijkstra, T., Chen, G., 2018. Investigating slow-moving landslides in the Zhouqu region of China using InSAR time series. Landslides 15 (7), 1299–1315.
Zheng, H., Shi, Z., Yu, S., Fan, X., Hanley, K.J., Feng, S., 2021. Erosion mechanisms of debris flow on the sediment bed. Water Resour. Res. 57 (12), 1–19.